The Astrophysical Journal, 762:59 (28pp), 2013 January 1 doi:10.1088/0004-637X/762/1/59

HerMES: CANDIDATE GRAVITATIONALLY LENSED GALAXIES AND LENSING STATISTICS AT SUBMILLIMETER WAVELENGTHS

Julie L. Wardlow[1], Asantha Cooray[1,2], Francesco De Bernardis[1], A. Amblard[3], V. Arumugam[4], H. Aussel[5], A. J. Baker[6], M. Béthermin[5,7], R. Blundell[8], J. Bock[2,9], A. Boselli[10], C. Bridge[2], V. Buat[10], D. Burgarella[10], R. S. Bussmann[8], A. Cabrera-Lavers[11,12,13], J. Calanog[1], J. M. Carpenter[2], C. M. Casey[14], N. Castro-Rodríguez[11,12], A. Cava[15], P. Chanial[5], E. Chapin[16], S. C. Chapman[17], D. L. Clements[18], A. Conley[19], P. Cox[20], C. D. Dowell[2,9], S. Dye[21], S. Eales[22], D. Farrah[23,24], P. Ferrero[11,12], A. Franceschini[25], D. T. Frayer[26], C. Frazer[1], Hai Fu[1], R. Gavazzi[27], J. Glenn[19,28], E. A. González Solares[17], M. Griffin[22], M. A. Gurwell[8], A. I. Harris[29], E. Hatziminaoglou[30], R. Hopwood[18], A. Hyde[18], E. Ibar[31], R. J. Ivison[4,31], S. Kim[1], G. Lagache[7], L. Levenson[2,9], L. Marchetti[25], G. Marsden[32], P. Martinez-Navajas[11,12], M. Negrello[25], R. Neri[20], H. T. Nguyen[2,9], B. O'Halloran[18], S. J. Oliver[23], A. Omont[27], M. J. Page[33], P. Panuzzo[5], A. Papageorgiou[22], C. P. Pearson[34,35], I. Pérez-Fournon[11,12], M. Pohlen[22], D. Riechers[2], D. Rigopoulou[34,36], I. G. Roseboom[4,23], M. Rowan-Robinson[18], B. Schulz[2,37], D. Scott[32], N. Scoville[2], N. Seymour[33,38], D. L. Shupe[2,37], A. J. Smith[23], A. Streblyanska[11,12], A. Strom[17], M. Symeonidis[33], M. Trichas[8], M. Vaccari[25,39], J. D. Vieira[2], M. Viero[2], L. Wang[23], C. K. Xu[2,37], L. Yan[2], and M. Zemcov[2,9]

[1] Department of Physics & Astronomy, University of California, Irvine, CA 92697, USA
[2] California Institute of Technology, 1200 E. California Blvd., Pasadena, CA 91125, USA
[3] NASA, Ames Research Center, Moffett Field, CA 94035, USA
[4] Institute for Astronomy, University of Edinburgh, Royal Observatory, Blackford Hill, Edinburgh EH9 3HJ, UK
[5] Laboratoire AIM-Paris-Saclay, CEA/DSM/Irfu-CNRS-Université Paris Diderot, CE-Saclay, pt courrier 131, F-91191 Gif-sur-Yvette, France
[6] Department of Physics and Astronomy, Rutgers, The State University of New Jersey, 136 Frelinghuysen Rd, Piscataway, NJ 08854, USA
[7] Institut d'Astrophysique Spatiale (IAS), bâtiment 121, Université Paris-Sud 11 and CNRS (UMR 8617), F-91405 Orsay, France
[8] Harvard-Smithsonian Center for Astrophysics, 60 Garden Street, Cambridge, MA 02138, USA
[9] Jet Propulsion Laboratory, 4800 Oak Grove Drive, Pasadena, CA 91109, USA
[10] Laboratoire d'Astrophysique de Marseille-LAM, Université Aix-Marseille & CNRS, UMR7326, 38 rue F. Joliot-Curie, F-13388 Marseille Cedex 13, France
[11] Instituto de Astrofísica de Canarias (IAC), E-38200 La Laguna, Tenerife, Spain
[12] Departamento de Astrofísica, Universidad de La Laguna (ULL), E-38205 La Laguna, Tenerife, Spain
[13] GTC Project, E-38205 La Laguna, Tenerife, Spain
[14] Institute for Astronomy, University of Hawaii, 2680 Woodlawn Drive, Honolulu, HI 96822, USA
[15] Departamento de Astrofísica, Facultad de CC. Físicas, Universidad Complutense de Madrid, E-28040 Madrid, Spain
[16] Herschel Science Centre, European Space Astronomy Centre, Villanueva de la Cañada, E-28691 Madrid, Spain
[17] Institute of Astronomy, University of Cambridge, Madingley Road, Cambridge CB3 0HA, UK
[18] Astrophysics Group, Imperial College London, Blackett Laboratory, Prince Consort Road, London SW7 2AZ, UK
[19] Center for Astrophysics and Space Astronomy 389-UCB, University of Colorado, Boulder, CO 80309, USA
[20] Institut de RadioAstronomie Millimétrique, 300 Rue de la Piscine, Domaine Universitaire, F-38406 Saint Martin d'Hères, France
[21] School of Physics and Astronomy, University of Nottingham, NG7 2RD, UK
[22] School of Physics and Astronomy, Cardiff University, Queens Buildings, The Parade, Cardiff CF24 3AA, UK
[23] Astronomy Centre, Department of Physics & Astronomy, University of Sussex, Brighton BN1 9QH, UK
[24] Department of Physics, Virginia Tech, Blacksburg, VA 24061, USA
[25] Dipartimento di Astronomia, Università di Padova, vicolo Osservatorio, 3, I-35122 Padova, Italy
[26] NRAO, P.O. Box 2, Green Bank, WV 24944, USA
[27] Institut d'Astrophysique de Paris, UMR 7095, CNRS, UPMC Univ. Paris 06, 98bis boulevard Arago, F-75014 Paris, France
[28] Department of Astrophysical and Planetary Sciences, CASA 389-UCB, University of Colorado, Boulder, CO 80309, USA
[29] Department of Astronomy, University of Maryland, College Park, MD 20742-2421, USA
[30] ESO, Karl-Schwarzschild-Str. 2, D-85748 Garching bei München, Germany
[31] UK Astronomy Technology Centre, Royal Observatory, Blackford Hill, Edinburgh EH9 3HJ, UK
[32] Department of Physics & Astronomy, University of British Columbia, 6224 Agricultural Road, Vancouver, BC V6T 1Z1, Canada
[33] Mullard Space Science Laboratory, University College London, Holmbury St. Mary, Dorking, Surrey RH5 6NT, UK
[34] RAL Space, Rutherford Appleton Laboratory, Chilton, Didcot, Oxfordshire OX11 0QX, UK
[35] Department of Physical Sciences, The Open University, Milton Keynes MK7 6AA, UK
[36] Department of Astrophysics, Denys Wilkinson Building, University of Oxford, Keble Road, Oxford OX1 3RH, UK
[37] Infrared Processing and Analysis Center, MS 100-22, California Institute of Technology, JPL, Pasadena, CA 91125, USA
[38] CSIRO Astronomy & Space Science, P.O. Box 76, Epping, NSW 1710, Australia
[39] Astrophysics Group, Physics Department, University of the Western Cape, Private Bag X17, 7535 Bellville, Cape Town, South Africa
Received 2012 May 16; accepted 2012 November 9; published 2012 December 14

ABSTRACT

We present a list of 13 candidate gravitationally lensed submillimeter galaxies (SMGs) from 95 deg^2 of the *Herschel* Multi-tiered Extragalactic Survey, a surface density of $0.14 \pm 0.04\,\mathrm{deg}^{-2}$. The selected sources have 500 μm flux densities (S_{500}) greater than 100 mJy. Gravitational lensing is confirmed by follow-up observations in 9 of the 13 systems (70%), and the lensing status of the four remaining sources is undetermined. We also present a supplementary sample of 29 ($0.31 \pm 0.06\,\mathrm{deg}^{-2}$) gravitationally lensed SMG candidates with $S_{500} = 80$–100 mJy, which are expected to contain a higher fraction of interlopers than the primary candidates. The number counts of the candidate lensed galaxies are consistent with a simple statistical model of the lensing rate, which uses a foreground matter distribution, the intrinsic SMG number counts, and an assumed SMG redshift distribution. The model predicts that 32%–74% of our $S_{500} \geqslant 100$ mJy candidates are strongly gravitationally lensed ($\mu \geqslant 2$), with the brightest sources being the most robust; this is consistent with the observational data. Our statistical model also

predicts that, on average, lensed galaxies with $S_{500} = 100$ mJy are magnified by factors of $\sim$9, with apparently brighter galaxies having progressively higher average magnification, due to the shape of the intrinsic number counts. 65% of the sources are expected to have intrinsic 500 μm flux densities less than 30 mJy. Thus, samples of strongly gravitationally lensed SMGs, such as those presented here, probe below the nominal *Herschel* detection limit at 500 μm. They are good targets for the detailed study of the physical conditions in distant dusty, star-forming galaxies, due to the lensing magnification, which can lead to spatial resolutions of $\sim$0.″01 in the source plane.

Key words: gravitational lensing: strong – submillimeter: galaxies

Online-only material: color figures

1. INTRODUCTION

Gravitational lensing increases the angular size and integrated flux of affected sources. It is exploited to investigate the mass distribution of the foreground lensing structures and the properties of the background lensed galaxies (see reviews by Bartelmann 2010; Treu 2010).

The magnification provided by gravitational lensing makes it an effective tool for identifying and studying intrinsically faint and typically distant galaxies (e.g., Stark et al. 2007; Richard et al. 2008, 2011). The flux boost from lensing yields an improved detection, and the associated spatial enhancement increases the ability to investigate the internal structure of distant galaxies to levels otherwise unattainable with the current generation of instrumentation (e.g., Riechers et al. 2008; Swinbank et al. 2010, 2011; Gladders et al. 2012). Furthermore, gravitational lensing probes the total mass of the foreground deflectors, including the relative content of dark and luminous mass. In combination with dynamical studies, lensing mass reconstruction allows one to obtain the density profile of the dark matter in individual lensing galaxies down to $\sim$10 kpc scales (e.g., Miralda-Escude 1995; Dalal & Kochanek 2002; Metcalf & Zhao 2002; Rusin & Kochanek 2005; Treu & Koopmans 2004).

The statistics of galaxy–galaxy lensing events, particularly the abundance of strongly lensed sources from a sample of galaxies with a known redshift distribution, can be used to constrain the global cosmological parameters, such as the cosmological constant. For example, the 28 lensed quasars in the Sloan Digital Sky Survey (SDSS) Quasar Lens Search (SQLS) led to an estimate of $\Omega_\Lambda = 0.74 \pm 0.17$, assuming a spatially flat universe (Oguri et al. 2012). A systematic search for large samples of lensed galaxies could provide constraints on cosmological parameters that are competitive with other cosmological probes (e.g., Marshall et al. 2009).

The past decade has seen dedicated optical and radio imaging and spectroscopic surveys for background sources strongly lensed by single foreground galaxies (the so-called strong galaxy–galaxy lensing). These include the Sloan Lens ACS Survey (Bolton et al. 2006), SQLS (Oguri et al. 2006), Strong Lens Legacy Survey (More et al. 2012; Ruff et al. 2011), and the BOSS Emission Line Lens Survey (Brownstein et al. 2012) in the optical and the Cosmic Lens All Sky Survey (CLASS; Browne et al. 2003). Unfortunately, in order to convert the lensing rate into a test of cosmological models, cosmological studies require that the selection function be simple and easy to describe. Furthermore, the initial selection of candidates is often inefficient, or the resulting targets are biased to low redshifts. For example, at radio wavelengths $\sim$0.2% of the initial targets of CLASS are lensed (Browne et al. 2003), although this can be improved to $\sim$2% by including SDSS information in the initial target selection (Jackson & Browne 2007). SDSS-based lensing searches are more efficient but are limited to lensed galaxies with $z \lesssim 0.7$ due to the survey depth (Treu & Koopmans 2004; Koopmans et al. 2006; Bolton et al. 2008a, 2008b; Auger et al. 2010; Brownstein et al. 2012).

It has long been proposed that large samples of gravitationally lensed, high-redshift galaxies can be efficiently selected by searching for bright sources in wide-area blank-field submillimeter surveys (e.g., Blain 1996; Perrotta et al. 2002; Negrello et al. 2007; Paciga et al. 2009). The unique advantage of selecting bright submillimeter sources as lensed galaxy candidates lies in the efficiency of this technique and the low contamination of samples. The number counts of distant submillimeter galaxies (SMGs) have intrinsically steep slopes at bright flux densities (e.g., Barger et al. 1999; Blain et al. 1999b; Coppin et al. 2006; Scott et al. 2006; Patanchon et al. 2009; Weiß et al. 2009b; Glenn et al. 2010; Oliver et al. 2010; Clements et al. 2010). Thus, a population of apparently bright 500 μm sources is expected to be dominated by gravitationally lensed sources, local late-type galaxies, and flat-spectrum radio quasars (or blazars; Negrello et al. 2007). The two contaminants can be easily removed by cross-identifying the bright submillimeter sources with shallow all-sky optical and radio surveys (e.g., Negrello et al. 2010).

With the launch of the *Herschel Space Observatory*[40] (Pilbratt et al. 2010), blank-field submillimeter surveys of hundreds of square degrees are being undertaken for the first time (e.g., Oliver et al. 2012; Eales et al. 2010), making systematic searches for strong galaxy–galaxy lensing practical. The first systematic *Herschel* survey for lensed SMGs was undertaken with *Herschel*-Astrophysical Terahertz Large Area Survey (H-ATLAS; Eales et al. 2010) Science Demonstration Phase (SDP) data. In that study Negrello et al. (2010) identified a total of 12 sources with 500 μm flux density, $S_{500} > 100$ mJy in 14.4 deg^2. Seven of the sources are associated with $z < 0.1$ late-type galaxies or radio-loud blazars, and the five remaining sources were confirmed as systems undergoing strong galaxy–galaxy lensing. Thus, Negrello et al. (2010) showed that one can reach $\sim$100% efficiency in the identification of strongly lensed galaxies, simply based on an observed submillimeter flux cut and existing all-sky survey data. The five H-ATLAS lensed systems have since been subject to extensive analysis and follow-up effort (Frayer et al. 2011; Hopwood et al. 2011; Lupu et al. 2012; Omont et al. 2011; Valtchanov et al. 2011).

Additional gravitationally lensed SMGs have since been identified in other extragalactic surveys with the Spectral and Photometric Imaging Receiver (SPIRE; Griffin et al. 2010; Swinyard et al. 2010) on *Herschel*. These include the $z = 2.957$ HerMES source, HLock01 (Section 6.7; Conley et al. 2011; Gavazzi et al. 2011; Riechers et al. 2011a; Scott et al. 2011), and

[40] *Herschel* is an ESA space observatory with science instruments provided by European-led Principal Investigator consortia and with important participation from NASA.

Table 1
Sources with $S_{500} \geqslant 80$ mJy in HerMES Blank Fields

Field[a]	R.A.[a]	Decl.[b]	Area[c] ($\deg^2$)	Lens Candidates ($S_{500} \geqslant 100$ mJy)		Blazars ($S_{500} \geqslant 80$ mJy)		Local Spirals ($S_{500} \geqslant 80$ mJy)		Faint Candidates ($S_{500} = 80$–100 mJy)	
				N	Density ($\deg^{-2}$)	N	Density ($\deg^{-2}$)	N	Density ($\deg^{-2}$)	N	Density ($\deg^{-2}$)
ELAIS-S1 SWIRE	$00^h35^m03^s$	$-43°34'42''$	8.6	0	<0.1	1	0.1 ± 0.1	4	0.5 ± 0.2	1	0.1 ± 0.1
XMM-LSS SWIRE	$02^h20^m36^s$	$-04°31'27''$	21.6	3	0.1 ± 0.1	0	<0.05	16	0.7 ± 0.2	10	0.5 ± 0.2
CDFS SWIRE	$03^h32^m05^s$	$-28°16'35''$	12.9	3	0.2 ± 0.1	1	0.1 ± 0.1	6	0.5 ± 0.2	3	0.2 ± 0.1
ADFS	$04^h43^m29^s$	$-53°51'09''$	8.6	0	<0.1	0	<0.1	7	0.8 ± 0.3	2	0.2 ± 0.2
COSMOS HerMES	$10^h00^m28^s$	$+02°12'55''$	3.3	0	<0.3	0	<0.3	2	0.6 ± 0.4	0	<0.3
Lockman SWIRE	$10^h48^m00^s$	$+58°09'02''$	18.2	4	0.2 ± 0.1	0	<0.1	16	0.9 ± 0.2	7	0.4 ± 0.1
EGS HerMES	$14^h20^m19^s$	$+52°48'56''$	3.1	0	<0.3	0	<0.3	0	<0.3	1	0.3 ± 0.3
Boötes NDWFS	$14^h32^m45^s$	$+34°10'10''$	11.3	3	0.3 ± 0.2	0	<0.1	12	1.1 ± 0.3	2	0.2 ± 0.2
FLS	$17^h15^m52^s$	$+59°23'15''$	7.3	0	<0.1	0	<0.1	12	1.6 ± 0.5	3	0.4 ± 0.2
Total	...	...	94.8	13	0.14 ± 0.04	2	0.02 ± 0.01	75	0.79 ± 0.09	29	0.31 ± 0.06

Notes.
[a] Field names correspond to those in Oliver et al. (2012).
[b] Coordinates are for the center of the HerMES field of view.
[c] The total area of pixels with any 500 μm coverage; same as $\Omega_{\rm max}$ in Oliver et al. (2012). This area is larger than the nominal HerMES coverage due to turnarounds and exact scan designs.

the H-ATLAS galaxies ID141 ($z = 4.24$; Cox et al. 2011) and HATLAS12–00 ($z = 3.259$; Fu et al. 2012). In addition, Harris et al. (2012) used CO ($J = 1 \rightarrow 0$) linewidths and integrated luminosities to show that 11 lensed galaxies from H-ATLAS are, on average, magnified by factors of 10, with a range of ~3–20 for individual sources. González-Nuevo et al. (2012) recently showed that *Herschel*-SPIRE data can be used to identify fainter lensed galaxies, although the selection process is necessarily more involved and will not be discussed further here. Outside of *Herschel*, a recent South Pole Telescope (SPT; Carlstrom et al. 2011) survey of the cosmological millimeter background identified 13 discrete sources in 87 $\deg^2$ that are consistent with gravitationally lensed galaxies at high redshift. These sources are detected at $>4.5\sigma$ (~15 mJy) at 1.4 mm, have 1.4–2.0 mm spectral indices consistent with thermal dust emission, and were not detected by *IRAS* (Vieira et al. 2010).

In order to build up large samples of strongly lensed SMGs, it is clearly necessary to test the supposition that high efficiency can be reached with only a flux cut and existing shallow optical and radio data. In this paper, we present a systematic survey for a sample of strongly lensed SMGs in ~95 $\deg^2$ of the *Herschel* Multi-tiered Extragalactic Survey[41] (HerMES; Oliver et al. 2012) data. In the ~95 $\deg^2$ of HerMES blank-field data 13 principal and 29 supplementary candidate lensed SMGs are identified. We describe a simple statistical lensing model, consisting of a foreground matter distribution and background SMGs, and show that the observed lensed number counts are consistent with the model prediction.

We have begun a follow-up multi-wavelength campaign to further understand the nature of the candidate lensed SMGs. Detailed observations of nine of the sources are presented, and these establish that they are all gravitationally lensed. Follow-up data are available for four of the 29 secondary candidates, of which only one is confirmed to be lensed, one is an intrinsically luminous galaxy, one is a blend of multiple sources in the *Herschel* beam, and the nature of the other is unclear.

In this paper, we focus on the ensemble properties of the primary lensed candidate list and consider statistics such as the lensing rate, number counts, and submillimeter color and redshift distributions of the lensed SMGs. In order to facilitate community participation in the follow-up observations, we also present the catalogs of our primary and secondary candidate lensed sources. Future publications will present detailed analysis of individual systems, including lensing mass models and properties of both the foreground and background galaxies, similar to the detailed presentation in Fu et al. (2012). The paper is organized as follows: The selection of the candidate gravitationally lensed galaxies is described in Section 2, and their basic properties are discussed in Section 3. In Section 4, we present a simple statistical model of the lensing rate and discuss the model predictions for the population of strongly lensed 500 μm selected sources. Follow-up data are described in Section 5, and lensed candidates are discussed on a source-by-source basis in Section 6. Individual supplementary candidate gravitationally lensed galaxies are discussed in the Appendix. Throughout this paper, we use J2000 coordinates and ΛCDM cosmology with $\Omega_{\rm M} = 0.27$, $\Omega_\Lambda = 0.73$, and $H_0 = 71\,{\rm km\,s^{-1}\,Mpc^{-1}}$. All photometry is on the AB magnitude system where 23.9 $m_{\rm AB} = 1\,\mu$Jy. For the purposes of our analysis we consider "strong" lensing as lensing in which the magnification factor, μ, is $\geqslant 2$.

2. IDENTIFICATION OF CANDIDATE LENSED GALAXIES

Candidate strongly lensed galaxies are selected from HerMES blank-field data[42] (see Oliver et al. 2012 for a full description of the HerMES survey). The total area considered for the candidate selection is 94.8 $\deg^2$ in nine independent fields (see Table 1). We employ the HerMES SPIRE imaging and photometry at 250, 350, and 500 μm in these fields. Sources are selected from HerMES catalogs (Smith et al. 2012; L. Wang et al. 2012, in preparation), which are extracted from the HerMES maps (Levenson et al. 2010).

We now briefly summarize details of the source detection and extraction procedure. Source detection is performed

[41] http://hermes.sussex.ac.uk/

[42] Publicly available HerMES data can be retrieved from http://hedam.oamp.fr/HerMES/

by StarFinder (Diolaiti et al. 2000) at 250 μm. StarFinder models the data as the summation of beam-smoothed point sources and iteratively detects, fits, and removes sources with decreasing brightnesses. StarFinder was designed to detect point sources in crowded fields, which results in a program that is good at deblending sources that are close together. This is important for our purposes because the blending of multiple sources in the SPIRE beam has the potential to mimic a single bright source, although we show in Section 4.3 that blending is not a concern for our sample. The opposite effect—whereby lensed galaxies with large separations between components are mistaken for blended sources—is not a significant issue for this work. This is because we only consider blank-field data, and not the regions around massive galaxy clusters. As such, most of the candidates are expected to be galaxy–galaxy lenses (e.g., HLock01), for which separations $\gtrsim$5″ (significantly smaller than the SPIRE beam: 18″, 25″, and 36″ FWHM at 250, 350 and 500 μm, respectively) are rare (Treu et al. 2010).

The 250, 350, and 500 μm flux densities of StarFinder 250 μm selected sources are extracted using the HerMES XID pipeline (Roseboom et al. 2010, 2012). XID allocates flux to sources on the basis of positional priors, which in this case are provided from StarFinder at 250 μm. Therefore, the source extraction algorithm uses the positional information at 250 μm, where the point-spread function is 18″ FWHM, to deblend sources at 350 and 500 μm. The use of the 250 μm positions as priors is not expected to bias our results against red, or high-redshift, galaxies because we are interested in the apparently brightest sources. For example, an Arp 220-like galaxy with $S_{500} = 80$ mJy at $z = 6$ will have $S_{250} \sim 30$ mJy and be detected in the 250 μm catalogs. Furthermore, the final step of the XID algorithm is to extract sources from the residual maps, so there is no a priori requirement for a 250 μm detection for inclusion in the catalog. Extended sources, such as local late-type galaxies, are fragmented into multiple components by the StarFinder+XID process outlined above. Therefore, for sources that are extended in the SPIRE beam, we make use of HerMES SUSSExtractor (Smith et al. 2012) flux densities, which are measured in large apertures.

The selection of candidate gravitationally lensed galaxies is performed at 500 μm, which is the SPIRE wavelength with the fewest expected contaminants (e.g., Negrello et al. 2007, 2010). Sources that are bright at 500 μm are typically either local ($z \lesssim 0.1$) late-type galaxies (e.g., Dunne et al. 2000; Serjeant & Harrison 2005), blazars (e.g., de Zotti et al. 2005; González-Nuevo et al. 2010), or gravitationally lensed SMGs (see also Negrello et al. 2007, 2010). Blazars are considered contaminants because the submillimeter emission is dominated by synchrotron radiation primarily from the radio jets. There may also be a contribution from intrinsically luminous SMGs; this contribution is strongly dependent on the 500 μm selection limit (Section 4.2).

We begin by identifying all sources with $S_{500} \geqslant 80$ mJy in the StarFinder+XID catalogs. At $z \gtrsim 1$ this flux density cut is equivalent to selecting only the most apparently far-IR luminous sources (with far-IR luminosity, $L_{\rm IR}$, $\gtrsim 6 \times 10^{12}\,L_{\odot}$ for an Arp 220 spectral energy distribution (SED), or $L_{\rm IR} \gtrsim 10^{13}\,L_{\odot}$ for an M82 SED or optically thin modified blackbody with $T_{\rm D} = 35$ K and $\beta = 1.5$). Thus, if they are not amplified by gravitational lensing, these sources are undergoing some of the most extreme growth in the universe (with star formation rate SFR $\gtrsim 1000\,M_{\odot}\,{\rm yr}^{-1}$; Kennicutt 1998).

Local late-type galaxies are identified by searching the NASA/IPAC Extragalactic Database[43] (NED) at the 250 μm positions of the $S_{500} \geqslant 80$ mJy sources. There are 75 bright local late-type galaxies, with $z < 0.1$, in the 94.8 deg^2 used for this study (Table 1). These sources form a separate population from traditional SMGs, which are dusty, star-bursting spheroidals, primarily at $z > 0.5$ (Lagache et al. 2003; Negrello et al. 2007). There is the chance of alignment between a background SMG and a local late-type galaxy. However, these local spirals are rare (0.8 deg^{-2}; Table 1), and the distance ratio of the background and foreground populations is such that they are not expected to act as strong gravitational lenses. Therefore, by removing the local late-type galaxies from the sample, we are not inadvertently removing a significant number of distant gravitationally lensed sources. Indeed, the local spirals have different distributions of submillimeter colors to the lensed candidates (Figures 1 and 2), which is indicative of two distinct populations at different redshifts.

Blazars are identified by searching for HerMES sources with associated radio emission in shallow, wide-area surveys (e.g., the NRAO VLA Sky Survey (NVSS), Condon et al. 1998; VLA Faint Images of the Radio Sky at Twenty-Centimeters, Becker et al. 1995; White et al. 1997; Parkes Radio Catalog, Wright et al. 1994), which we access using NED. There are two bright HerMES sources with $S_{500} > 80$ mJy that are associated with bright radio emission; these are 1HERMES S250 J003017.4−422443 and 1HERMES S250 J032752.0−290908 (Table 2).

We determine whether the radio emission could be the result of star formation, rather than active galactic nucleus (AGN) activity, by comparing the observed radio flux with that predicted from the far-IR/radio correlation. The calculation is performed for $q_{\rm IR} = 2.40 \pm 0.24$ (Ivison et al. 2010a), where

$$q_{\rm IR} = \log_{10}(L_{\rm IR}/3.75 \times 10^{12}\,{\rm W}) - \log_{10}(L_{1.4}/{\rm WHz}^{-2}). \quad (1)$$

$L_{\rm IR}$ is the rest-frame 8–1000 μm luminosity, determined from the HerMES photometry, and $L_{1.4}$ is rest-frame 1.4 GHz radio luminosity density. Radio luminosities are K-corrected assuming $S_{\nu} \propto \nu^{\alpha}$, with $\alpha = -0.8$.

A 4.85 GHz flux density of 0.5 mJy is predicted for 1HERMES S250 J003017.4−422443 at $z = 0.495$, which is ∼900 times lower than the observed radio flux density of 420 mJy. Thus, we conclude that 1HERMES S250 J003017.4−422443 is a blazar, and it is excluded from our sample. This classification is confirmed by the X-ray (*ROSAT*; Voges et al. 1999) and gamma-ray (*Fermi*; Abdo et al. 2009) detections of 1HERMES S250 J003017.4−422443 and its identification as a quasar by Hewitt & Burbidge (1989).

The other radio-detected source, 1HERMES S250 J032752.0−290908, does not have an available archival redshift. Instead, we fit cold dust SEDs, of the same form as Arp 220, M82, and HR10 (Silva et al. 1998), to the SPIRE photometry, to estimate $z \sim 4.5$, if the far-IR emission is star formation dominated. This assumption is also required for the far-IR/radio correlation; therefore, if the far-IR/radio correlation holds, then the photometric redshift should also be reasonable. For $z = 4.5$, the predicted radio flux density for 1HERMES S250 J032752.0−290908 is 0.13 mJy at 1.4 GHz, which is ∼170 times lower than observed. Therefore, we conclude that 1HERMES S250 J032752.0−290908 is also a blazar and the photometric redshift estimate from the far-IR/submillimeter

[43] http://www1.ned.ipac.caltech.edu/

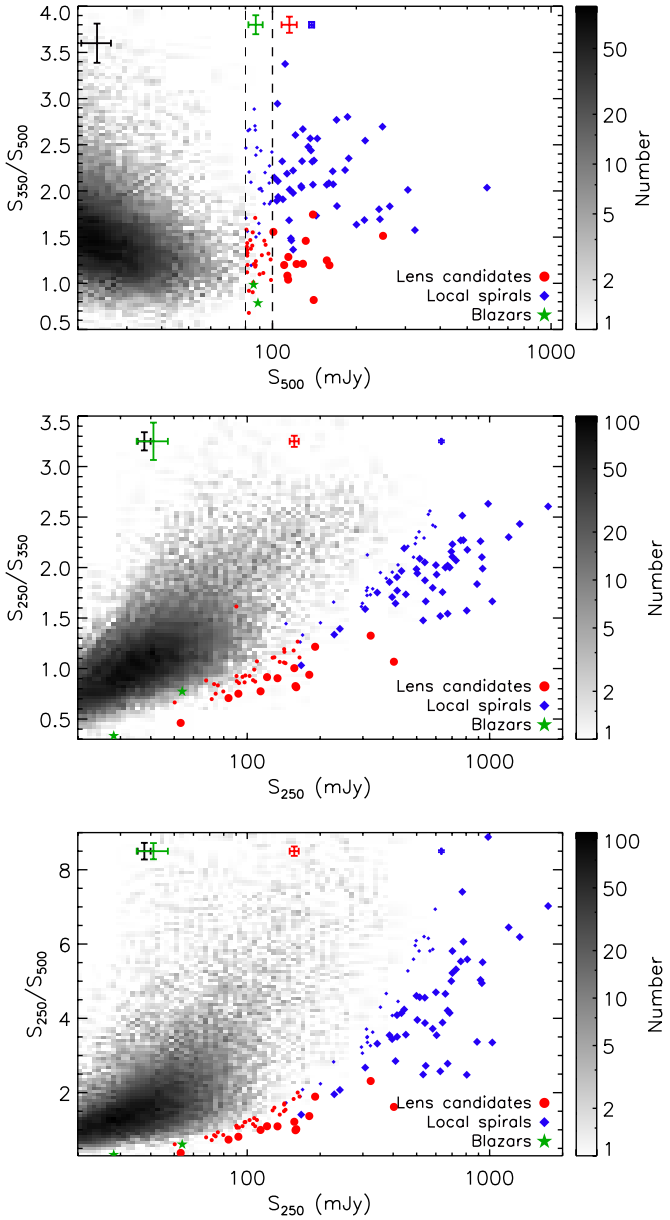

Figure 1. SPIRE color-flux density plots for sources detected in HerMES blank fields. Sources brighter than 80 mJy at 500 μm are highlighted and classified as blazars, local late-type galaxies, or candidate gravitationally lensed SMGs (see Section 2 for details). Large and small symbols correspond to sources with $S_{500} > 100$ mJy (robust lensed candidates) and $S_{500} = 80$–100 mJy (supplementary lensed candidates), respectively. Gray-scale data represent the density of all HerMES sources in these fields. Candidate gravitationally lensed SMGs have redder SPIRE colors than local late-type galaxies, indicating that they are typically higher redshift sources. Median error bars for the individual populations are shown at the top of each panel, at the median flux density of each population. We note that the apparent offset in SPIRE color-flux density space of the highlighted sources compared to the bulk of the HerMES population is due to our selection of the brightest sources. Indeed, in SPIRE color–color space no such offset is apparent (Figure 2).

(A color version of this figure is available in the online journal.)

SED is incorrect. It is also removed from the sample of candidate gravitationally lensed SMGs.

Finally, the star Mira (o Ceti) is in the XMM-LSS SWIRE field and has $S_{500} > 80$ mJy, and it too is removed from our analysis (see also Mayer et al. 2011). There are no other submillimeter-luminous stars in the data. The associations between the HerMES sources with $S_{500} \geqslant 80$ mJy and local late-type galaxies, AGNs, and Mira are confirmed by eye, and a thorough inspection of the data affirms that there is no ambiguity as to the validity of any of these associations.

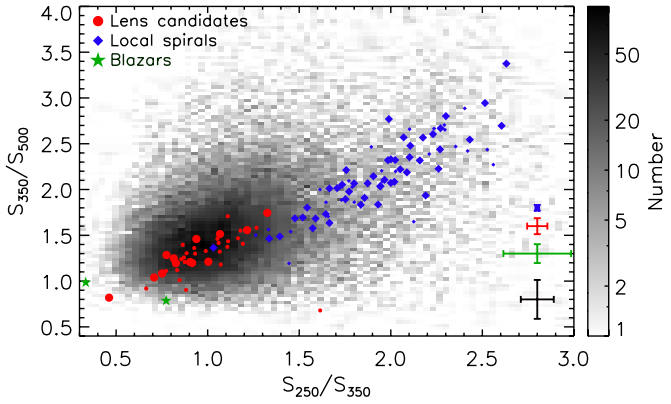

Figure 2. SPIRE color–color diagram for sources detected in HerMES blank fields. Candidate lensed galaxies, blazars, and bright local spirals are highlighted; large and small symbols signify sources with $S_{500} > 100$ mJy and $S_{500} = 80$–100 mJy, corresponding to the principal and supplementary samples, respectively. The gray-scale data show the density of all HerMES sources in these fields. The lensing candidates have submillimeter colors that are consistent with the rest of the SPIRE population. Median error bars for each population are shown at the bottom right.

(A color version of this figure is available in the online journal.)

Having removed the 78 contaminants described above from the initial list, 42 sources remain. There are 13 with $S_{500} > 100$ mJy, which compose our primary sample of robust candidate gravitationally lensed HerMES galaxies (discussed individually in Section 6). The remaining 29 sources have $S_{500} = 80$–100 mJy and make up the supplementary sample. The division at 100 mJy between the robust and supplementary sample is made on the basis of the 500 μm number counts (Figure 6) and is supported by the fraction of lensed sources that is predicted by modeling (Section 4.1). The distribution of the candidates between the nine survey fields is shown in Table 1, and a list of all the candidates and their 250, 350, and 500 μm flux densities are presented in Table 4. Additional archival and follow-up infrared and radio photometry is listed in Table 5.

The surface density of the main ($S_{500} > 100$ mJy) and supplementary samples ($S_{500} = 80$–100 mJy) of lensing candidates is 0.14 ± 0.04 deg^{-2} and 0.31 ± 0.06 deg^{-2}, respectively. For comparison, Negrello et al. (2010) identified five candidate lensed galaxies with $S_{500} > 100$ mJy in 14.4 deg^2 (0.35 ± 0.16 deg^{-2}) of the H-ATLAS SDP area (all five are confirmed to be lensed), and 13 candidate lensed galaxies were identified at $>4.5\sigma$ ($\sim$15 mJy) at 1.4 mm in 87deg^2 of SPT data (0.15 deg^{-2}; Vieira et al. 2010). The number density of HerMES lens candidates is lower than the H-ATLAS SDP area from Negrello et al. (2010), but the difference is not statistically significant.

3. PROPERTIES OF CANDIDATE STRONGLY LENSED SMGs

Having identified 13 robust and 29 supplementary candidate gravitationally lensed SMGs, we next consider the basic properties of these sources, including their submillimeter colors (Section 3.1), redshifts (Section 3.2), and apparent luminosities (Section 3.3).

3.1. SPIRE Colors

Figure 1 shows *Herschel* SPIRE 250, 350, and 500 μm color-flux density plots for sources in HerMES blank fields. Candidate lensed SMGs presented in this paper are highlighted,

Table 2
Blazars with $S_{500} \geqslant 80$ mJy in the HerMES Fields

HerMES source	Name[a]	S_{250} (mJy)	S_{350} (mJy)	S_{500} (mJy)	Observed Radio Flux (mJy)	Predicted Radio Flux[b] (mJy)	z
1HERMES S250 J003017.4−422443	[HB89] 0027−426[c]	54 ± 6	70 ± 5	89 ± 5	419 ± 23[d]	0.5	0.495[c]
1HERMES S250 J032752.0−290908	NVSS J032752−290912[e]	28 ± 6	84 ± 4	86 ± 5	23.1 ± 1.1[f]	0.1	...

Notes.
[a] The name of the associated blazar from NED.
[b] The predicted radio flux is calculated from the far-IR radio correlation, assuming that the radio emission is from star formation (see the text for details).
[c] Hewitt & Burbidge (1989), Wright et al. (1994), Massaro et al. (2009), and Jackson et al. (2002).
[d] The radio flux measurement for [HB89] 0027−426 is at 4.85 GHz.
[e] Condon et al. (1998).
[f] The radio flux measurement for NVSS J032752−290912 is at 1.4 GHz.

and local late-type galaxies and blazars that are brighter than 80 mJy at 500 μm are also identified. As discussed in Section 2, the StarFinder+XID catalogs are used for blazars and candidate lensed galaxy flux densities, whereas the flux densities of local late-type galaxies are from the SUSSExtractor catalog, which is more reliable for extended sources.

The principal sample of lensed SMG candidates has median $S_{250}/S_{350} = 0.90$ ($\sigma = 0.22$), $S_{350}/S_{500} = 1.21$ ($\sigma = 0.24$), and $S_{250}/S_{500} = 1.09$ ($\sigma = 0.51$). These colors are comparable to the background SMG population ($S_{250}/S_{350} = 1.07$, $S_{350}/S_{500} = 1.51$, and $S_{250}/S_{500} = 1.60$, with $\sigma = 0.37$, 1.02, and 1.67, respectively). There is a hint that the candidate lensed sources may be slightly redder than the background. As expected, the local spiral galaxies have significantly bluer colors than both the candidate lensed galaxies and the background SPIRE population, with median $S_{250}/S_{350} = 1.97$ ($\sigma = 0.33$), $S_{350}/S_{500} = 2.08$ ($\sigma = 0.42$), and $S_{250}/S_{500} = 4.14$ ($\sigma = 1.48$) for the $S_{500} \geqslant 100$ mJy subset. These colors also indicate that the candidate lensed galaxies lie at higher redshifts than local spiral galaxies with similar 500 μm flux densities.

The candidate lensed sources, local spirals, and blazars appear offset in S_{250}–S_{250}/S_{350} and S_{250}–S_{250}/S_{500} color-flux density spaces compared to the background of HerMES sources (Figure 1). This is because the highlighted sources are bright at 250 μm, which is a direct result of the flux selection at 500 μm. Indeed, the color–color diagram (Figure 2) shows that the lensing candidates have colors consistent with the HerMES background population, while local spiral galaxies have colors that are bluer than the majority of sources.

There are two lensed galaxy candidates that have bluer submillimeter colors than the majority. Both of these sources are known to be strongly gravitationally lensed (HBoötes03, Borys et al. 2006, Section 6.3; and HLock01, Conley et al. 2011, Section 6.7). It is possible that differential magnification could affect the submillimeter colors of these galaxies (e.g., Hezaveh et al. 2012; Serjeant 2012), although cold dust dominates the emission at 250–500 μm, so the effect is likely to be minor. We conclude that although the candidate gravitationally lensed galaxies are typically redder at submillimeter wavelengths than local late-type galaxies, there are some exceptions, and a color selection is not sufficient to identify local interlopers. Instead, the removal of interlopers requires the additional information that is provided by optical and radio data, which can be provided by existing shallow surveys (see Section 2).

3.2. Redshift Distribution

We have shown that the candidate lensed SMGs have redder submillimeter colors than local spiral galaxies, which is indicative of a higher redshift population. We next consider the full redshift distributions of these sources.

There are four main ways to calculate the redshifts of SMGs. The most reliable is through the detection of submillimeter emission lines, the brightest of which are CO transitions. The second method is to calculate submillimeter photometric redshifts from the 250, 350, and 500 μm photometry and any available longer wavelength data (Table 5). Finally, optical or near-IR photometry or spectroscopy of the counterparts can be utilized. However, if an SMG is gravitationally lensed, then the foreground deflector will usually dominate the short-wavelength flux. In this case, if the foreground lens is misidentified as the SMG, then the optical redshift will be lower than the submillimeter redshift.

We are currently undertaking an extensive radio and millimeter spectroscopic follow-up campaign, targeting CO emission lines in the candidate gravitationally lensed galaxies (see Section 5.2 for details). Confirmed (multiple-line) redshifts have been obtained for five of the candidate lensed SMGs, and single-line redshifts for a further four (Table 4; D. Riechers et al. 2012, in preparation). The single-line CO redshifts are guided by the photometric redshifts in determining the most likely identification of the line emission.

Submillimeter photometric redshifts are calculated from χ^2 template fitting to the available submillimeter and millimeter data. The SED of SMM J2135−0102 (the Cosmic Eyelash; Ivison et al. 2010b; Swinbank et al. 2010) is used as the reference template, because Harris et al. (2012) showed that it is representative of *Herschel* lensed galaxies with Robert C. Byrd Green Bank Telescope (GBT) detections of CO($J = 1 \rightarrow 0$). The analysis is restricted to a single template because Harris et al. (2012) also showed that χ^2 fitting to the SPIRE data alone is unable to effectively select between multiple SEDs. We caution that the template choice results in a potential bias in the submillimeter photometric redshifts, due to the assumption that each source has an intrinsic SED (and dust temperature, T_D) that is similar to SMM J2135−0102. We assign each photometric redshift an error of ± 0.25, which was shown empirically by Harris et al. (2012) to account for statistical

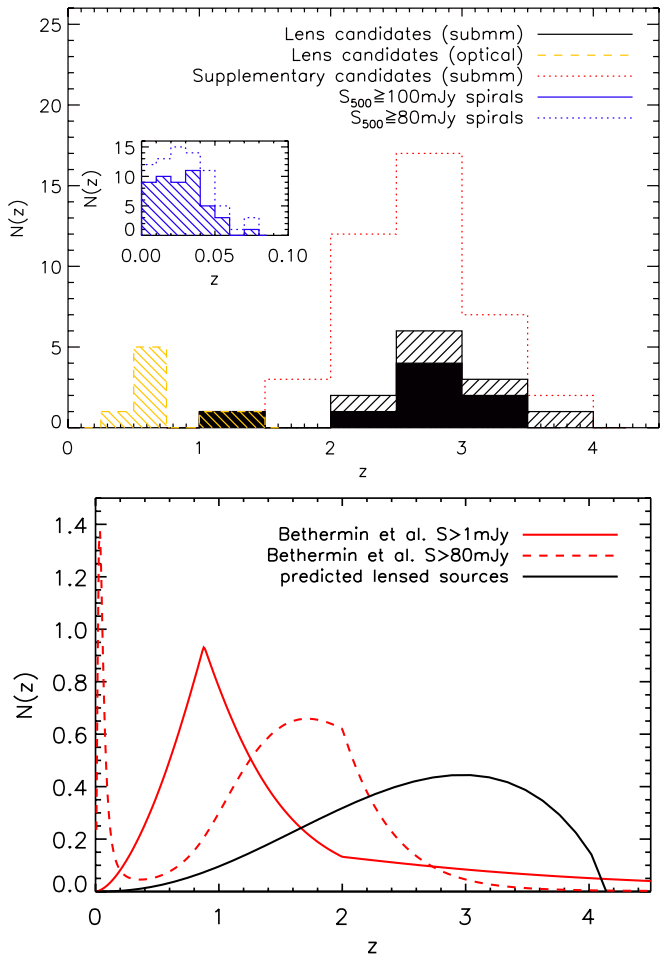

Figure 3. Top: redshift distribution of HerMES lens candidates and (inset) bright local late-type galaxies. Where possible, submillimeter redshifts are derived from the detection of one or more CO emission lines (solid histogram for the robust sample); otherwise, submillimeter photometric redshifts are used. Optical redshifts trace the confirmed foreground lenses. The background SMGs are typically at $z_{\rm submm} = 2.8$ (mean and median) and are lensed by sources at $z_{\rm opt} \sim 0.7$ (mean $z_{\rm opt} = 0.72$; median $z_{\rm opt} = 0.60$). We note that the redshift distribution of the supplementary sample of lens candidates is consistent with the principal sample. The local late-type galaxies are all at $z < 0.1$ and peak at $z = 0.028$, confirming that they are easily identified in shallow all-sky surveys (Section 2). Bottom: normalized redshift distribution of theoretical SMG populations, and the prediction from our model for the distribution of gravitationally lensed galaxies (Section 4). The predicted redshift distribution of strongly lensed SMGs is not a random sampling of the input populations due to the optical depth to lensing. The model predicts that the redshift distribution of lensed SMGs peaks at $z \sim 3$, which is in broad agreement with available data, although confirmation requires a larger sample.

(A color version of this figure is available in the online journal.)

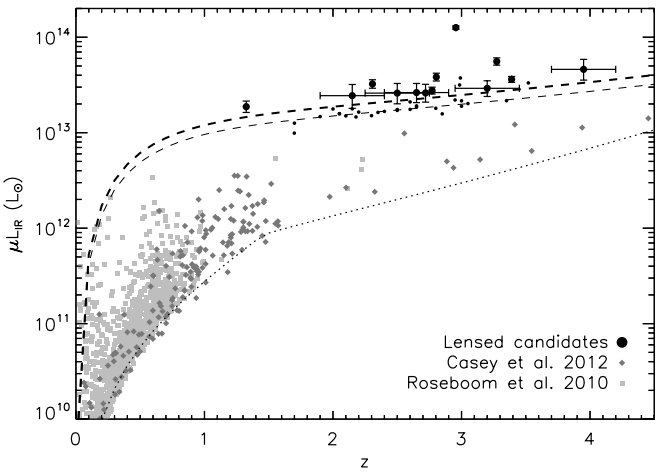

Figure 4. Apparent rest-frame 8–1000 μm infrared luminosity as a function of redshift for HerMES sources, *assuming no lensing magnification*. Large and small symbols represent our principal and supplementary candidates, respectively. Due to the selection of the brightest 500 μm sources, the candidate gravitationally lensed galaxies appear significantly more luminous than a comparison sample of "normal" (assumed not to be lensed) HerMES sources (Roseboom et al. 2010; Casey et al. 2012). The curved lines represent the *approximate* selection limits for the samples: the two upper lines (dashed) represent the candidate lensed SMG selection and are the luminosities of an optically thin, $T_{\rm D} = 35$ K modified blackbody with observed 500 μm flux densities of 100 and 80 mJy (thick and thin, respectively, corresponding to the principal and supplementary candidates, respectively). The lower line (dotted) represents the selection of sources in the two comparison samples, as described in the text. Error bars are omitted from the supplementary candidates and the comparison samples for clarity.

errors, the uncertainty in the choice of SED template, and the implicit assumption that differential magnification between these wavelengths is unimportant. The redshift error is not required for our analysis and is only used for display purposes in Figure 4.

In Figure 3 (top panel), we show the redshift distributions of the candidate lensed galaxies, as derived from submillimeter and optical data; CO redshifts are preferred where available. The optical redshift distribution peaks at $z_{\rm opt} = 0.60$ (median; mean $z_{\rm opt} = 0.72$), and as expected, the submillimeter-derived redshifts peak at a higher value—$z_{\rm submm} = 2.8$ (median and mean). Thus, on average the HerMES lensed SMGs lie at $z \sim 2.8$ and are magnified by sources at $z \sim 0.7$. We note that submillimeter redshifts of the supplementary sample are similar to those of the primary lensed candidates. In the inset in Figure 3 (top panel), we also show the distribution of local late-type galaxies, identified in Section 2. All of the submillimeter-luminous local galaxies are at $z < 0.1$, with a median of $z = 0.028$, confirming that they are easily distinguished from the SMGs.

For comparison, the bottom panel of Figure 3 shows the redshift distribution of unlensed submillimeter sources in the Béthermin et al. (2011) model. Both models depend on the flux limits assumed, so we show sources with $S_{500} \geqslant 80$ mJy and $S_{500} \geqslant 1$ mJy separately. We note that, as observed in the HerMES data, at the bright flux limit the models contain a population of $z \ll 1$ spiral galaxies in addition to the higher redshift SMGs. Figure 3 (bottom panel) also contains the redshift distribution of strongly gravitationally lensed SMGs as predicted by our model (Section 4.2). The predicted redshift distribution peaks at $z \sim 3$, in broad agreement with the HerMES candidates. The redshift distribution of lensed sources is not a random sampling of the parent SMG population because the optical depth to lensing is also important.

3.3. Apparent Luminosity Distribution

We next consider the apparent far-IR luminosities of the HerMES candidate gravitationally lensed SMGs. In Figure 4, we show the distribution of redshift against apparent infrared (rest-frame 8–1000 μm) luminosity (i.e., assuming no lensing magnification) for the candidate gravitationally lensed sources. The infrared luminosities are calculated by fitting an optically thin modified blackbody, with fixed dust emissivity, $\beta = 1.5$, to the available submillimeter and millimeter data (Table 5).

For comparison, we also show ~1300 HerMES sources with optical and near-IR redshifts from a dedicated optical

spectroscopic follow-up program (Casey et al. 2012) and those in the Boötes field with archival optical spectroscopic and photometric redshifts. The optical counterparts for both comparison samples are identified according to the method described in Roseboom et al. (2010), and we require that the sources are detected at $>3\sigma$ in all three SPIRE bands (250, 350, and 500 μm), so that the infrared luminosities can be reliably determined.

We also show the approximate selection limits in Figure 4, which for the lensed candidate samples are calculated assuming $T_{\rm D} = 35$ K and $S_{500} = 100$ mJy ($S_{500} = 80$ mJy for the supplementary sample). The selection of the comparison sources is complicated because it is driven by different wavelengths at different redshifts. In this case, we follow Casey et al. (2012) and use the minimum of three optically thin modified blackbodies—with $T_{\rm D} = 20$ K and $S_{250} = 15$ mJy, $T_{\rm D} = 30$ K and $S_{350} = 15$ mJy, and $T_{\rm D} = 50$ K and $S_{500} = 15$ mJy.

The candidate gravitationally lensed sources are at $z \sim 1$–4 and have apparent infrared luminosities between 1.9×10^{13} and $1.3 \times 10^{14}\,\mu^{-1}\,L_{\odot}$, with a median of $2.9 \times 10^{13}\,\mu^{-1}\,L_{\odot}$, where μ is the magnification factor from gravitational lensing. This median infrared luminosity corresponds to a star formation rate of $\sim$5500 $\mu^{-1}\,M_{\odot}\,{\rm yr}^{-1}$ (Kennicutt 1998), which represents some of the most extreme star formation episodes in the universe, unless the amplification from gravitational lensing is large. We note that, despite the flux selection, some of the supplementary lensed candidates are more infrared-luminous than some members of the principal sample because of the variation in $T_{\rm D}$ between the galaxies.

The comparison sample of HerMES sources with known redshifts has a median infrared luminosity of $6.9 \times 10^{10}\,L_{\odot}$. However, these values are not directly comparable with the candidate lensed SMGs because 95% of the comparison sample is at $z < 1$. The trend to low redshift is not indicative of the redshift distribution of SPIRE-selected galaxy populations but is due to the inherent biases in archival surveys (see Casey et al. 2012 for a detailed discussion). If we only consider the 73 sources in the comparison sample with $z > 1$, the median infrared luminosity is $1.5 \times 10^{12}\,L_{\odot}$ (SFR $\sim 260\,M_{\odot}\,{\rm yr}^{-1}$), which is still significantly lower than the candidate gravitationally lensed sources. As illustrated in Figure 4, this difference is a direct result of a combination of our source selection technique, which identifies candidates on the basis of bright 500 μm flux densities (Section 2), and the relatively flat K-correction for $z \gtrsim 0.5$ at 500 μm.

4. LENSING STATISTICS AT SUBMILLIMETER WAVELENGTHS

Submillimeter-selected populations have steep number counts at the bright end, and therefore the gravitational lensing of SMGs leads to a change in the observed counts (e.g., Blain 1996; Negrello et al. 2007; Jain & Lima 2011). The intrinsic slope of the luminosity function of the population targeted determines whether lensing will affect the observed counts and luminosity function. For example, gravitational lensing does not significantly affect the observed luminosity functions of radio-selected sources (Peacock 1982).

In this section, we use the HerMES observed 500 μm number counts to constrain a statistical model of the effect of flux boosting. The model is described in Section 4.1, and in Section 4.2 we use it to predict additional properties of the lensed galaxies, including the expected mean magnification and fraction of candidates that are strongly lensed. In Section 4.3, we show that the effect of source blending—whereby multiple SMGs contribute to the flux in a single SPIRE beam—is negligible.

Similar analyses have recently been undertaken for sources detected in the SPT and BLAST surveys, using both analytic models (Lima et al. 2010a, 2010b) and ray-tracing simulations (Hezaveh & Holder 2011). Both ray-tracing (Lapi et al. 2012) and analytical modeling (Short et al. 2012) of lensed H-ATLAS sources have also been performed. Likewise, Paciga et al. (2009) used constraints from existing SCUBA data to predict the number of lensed sources likely to be detected in upcoming 850 μm SCUBA-2 surveys. We reiterate that a substantial fraction of the brightest 500 μm sources are local late-type galaxies and thus a lensing model need not account for all of the bright sources (see Lima et al. 2010a).

4.1. Modeling the Lensed SMG Population

Existing literature discusses the details of the lensing calculations that are undertaken here (e.g., Perrotta et al. 2002; Negrello et al. 2007). Therefore, in this section we provide a summary of the calculations performed and refer to the appropriate papers for the details.

Briefly, the calculation consists of the following processes and assumptions:

1. *Foreground mass profile.* Consider foreground masses with Navarro et al. (1997, NFW) or single isothermal sphere (SIS) profiles. The effect of the choice of mass profile is discussed in Section 4.2.
2. *Spatial distribution of foreground lenses.* Determine the comoving number density of foreground lenses as a function of mass and redshift, using the Sheth & Tormen (1999) relation.
3. *Redshift distribution of SMGs.* Use the model of Béthermin et al. (2011), with $S_{500} > 1$ mJy, to trace the redshift distribution of the intrinsic (unlensed) population of SMGs (Figure 3; bottom panel).
4. *Strongly lensed area.* Calculate the fraction of the sky (f_{μ}) that is strongly lensed ($\mu > \mu_{\rm min}$, for $\mu_{\rm min} = 2$), using the profile and distribution of foreground masses and the redshift distribution of SMGs.
5. *Intrinsic population.* Assume that the shape of the intrinsic (unlensed) number counts has the form of a Schechter (1976) function. Although other choices may be suitable, this function adequately describes the observed data with only three free parameters.
6. *Perform the magnification.* Integrate and apply the lensing probability to the intrinsic flux distribution to determine the net effect of lensing. The limits of the integration are set to $\mu_{\rm min} = 2$ (for strong lensing) and $\mu_{\rm max} = 50$ (for feasible sizes of the submillimeter emission regions).
7. *Fitting.* Use a Monte Carlo Markov chain (MCMC) minimization technique to fit the total HerMES counts with the four model components: unlensed SMGs, lensed SMGs, blazars, and local late-type galaxies.
8. *Predictions.* Use the fitted model to predict properties of strongly lensed SMGs, including their number counts and mean magnification (see Section 4.2).

We begin by considering the properties of the foreground (lensing) structures. The effect of gravitational lensing on the submillimeter number counts can be quantified when specific assumptions about the foreground masses are made. Virialized

dark matter halos have an NFW universal density (ρ) profile, which is a function of radius, r:

$$\rho(r) = \frac{\rho_s}{(cr/r_{vir})(1+cr/r_{vir})^2}, \quad (2)$$

where r_{vir} is the virial radius and ρ_s is the characteristic density (Navarro et al. 1997). The halo concentration parameter, c, describes how centrally concentrated the mass is and can be obtained from a fit to simulations (e.g., Bullock et al. 2001):

$$c(M_{vir}, z) = \frac{9}{1+z}\left(\frac{M_{vir}}{M_*}\right)^{-0.13}, \quad (3)$$

where M_* is the mass value such that $\sigma(M_*) = \delta_c$ and $\sigma^2(M)$ is the variance of the linear density field. M_{vir} is the virial mass of a dark matter halo, and δ_c is the critical density contrast for the spherical collapse model (Gunn & Gott 1972; Lacey & Cole 1993). Since δ_c has only a very mild redshift and cosmology dependence, here we take it to be fixed at the value for a matter-dominated universe, i.e., $\delta_c = 1.686$.

While the NFW profile is the observed density profile of dark matter halos, gravitational lensing captures the total mass. Existing lensing analysis of individual galaxy- and group-scale lenses shows that the total density profile is more consistent with an SIS parameterization (e.g., Kochanek 1995; Koopmans et al. 2006, 2009; Gavazzi et al. 2007; Barnabè et al. 2010; Ruff et al. 2011; Bolton et al. 2012). Thus, as an alternative choice, we also consider the SIS density profile:

$$\rho(r) = \frac{\sigma_v^2}{2\pi G r^2}, \quad (4)$$

where σ_v^2 is the line-of-sight velocity dispersion, calculated following Perrotta et al. (2002). The SIS profile offers many advantages due to the simplicity of its form, and Perrotta et al. (2002) showed that the SIS and NFW profiles provide similar results for statistical magnifications. Indeed, as discussed in Section 4.2, we find that the uncertainties in the overall modeling are such that we cannot reliably distinguish the lensing by NFW halos and SIS spheres using the HerMES data presented here. However, detailed analysis of individual systems may be able to distinguish one profile over another on a case-by-case basis. Given the limited statistics, we do not account for sub-halo masses (e.g., Oguri et al. 2006), the effect of edge-on spirals as lenses (e.g., Blain et al. 1999a), or more complicated issues such as galaxy/dark matter halo ellipticity and external shear. Our predictions are in agreement with the current data, but in wider area surveys with more statistics it may become feasible to constrain these additional effects. We refer the reader to Oguri et al. (2006) for more detail of these effects in calculations of gravitational lensing rates.

The projected density field, Σ, around each mass profile is obtained by integrating over the parallel component, $r_\parallel = \chi$, of the position vector $\bar{x} = (r_\parallel, r_\perp)$, where the perpendicular coordinate is $r_\perp = D_A(\chi)\theta$, with D_A being the angular diameter distance, θ being the angular coordinate in the lens plane, and χ being the comoving radial distance. The convergence term, κ, associated with the isotropic light distortion from gravitational lensing can then be defined in terms of the critical density, Σ_{crit} (Lima et al. 2010a):

$$\kappa(\theta) = \frac{\Sigma(\theta)}{\Sigma_{crit}}, \quad (5)$$

$$\Sigma_{crit} = \frac{a}{4\pi G}\frac{D_A(\chi_s)}{D_A(\chi)D_A(\chi_s - \chi)}, \quad (6)$$

where $a = (1+z)^{-1}$ is the cosmological scale factor and χ_s is the comoving radial distance to the source. The anisotropic distortion from lensing is measured by the shear, $\boldsymbol{\gamma} = \gamma_1 + i\gamma_2$, where γ_i are the two components of the shear matrix. The magnitude of shear depends on the shape of the density profile of the foreground mass. For the NFW profile it is (Takada & Jain 2003)

$$\gamma_{NFW}(\theta) = \frac{M_{vir} f(c) c^2}{2\pi r_{vir}^2}\frac{g(c\theta/\theta_{vir})}{\Sigma_{crit}}, \quad (7)$$

where $g(x)$ is a function that can be calculated analytically (see Lima et al. 2010a for details) and $f(c) = (\ln(1+c) - c/(1+c))^{-1}$.

For the SIS profile all the quantities can be derived analytically, and the resulting shear is

$$\gamma_{SIS}(\theta) = 4\pi\sigma_v^2\frac{D_A(\chi_s - \chi)}{D_A(\chi_s)}\frac{1}{2\theta}. \quad (8)$$

Gravitational lensing causes a flux amplification due to an increase in the angular size of source galaxies. This effect is measured by the magnification factor, μ, which is given by the inverse determinant of the Jacobian matrix describing the transformation between source and image angular coordinates. In terms of the convergence and shear we have

$$\mu(\theta) = \frac{1}{[1-\kappa(\theta)]^2 - |\gamma(\theta)|^2}. \quad (9)$$

A halo with mass, M, and at redshift, z_l, magnifies a source at redshift, z_s, in an elliptical region of the image plane with area, $\Delta\Omega_\mu(z_l, z_s, M, \mu_{min})$, within which the magnification is larger than μ_{min}:

$$\Delta\Omega_\mu(\mu_{min}) = \int_{\mu(\theta)>\mu_{min}} \frac{d\theta^2}{\mu(\theta)}, \quad (10)$$

where we set $\mu_{min} = 2$ for strong gravitational lensing.

For a known distribution of foreground masses, it is possible to define a fraction, f_μ, of the sky where $\mu > \mu_{min}$ due to all the halos above a certain mass and in a redshift range. f_μ will therefore depend on the comoving number density of halos, defined as

$$\frac{dn}{d\ln M_{vir}} = \frac{\rho_m}{M_{vir}} f(\nu)\frac{d\nu}{d\ln M_{vir}}, \quad (11)$$

where $\nu = \delta_c/\sigma(M_{vir})$ and $\sigma^2(M)$ is the variance in a top hat of radius, r. Here, we use the Sheth & Tormen (1999) relation:

$$\nu f(\nu) = A\sqrt{\frac{2}{\pi}a\nu^2}[1 + (a\nu^2)^{-p}]\exp[-a\nu^2/2]. \quad (12)$$

We take the parameter values $p = 0.3$, $a = 0.75$, and $A \simeq 0.3222$ as normalization constants (Cooray & Sheth 2002). We have then

$$f_\mu = \int_0^{z_s} dz_l \frac{D_A^2(z_l)}{H(z_l)} \int_{M_{min}}^{M_{max}} d\ln M_{vir} \int_0^\infty dz_s P(z_s) \times \Delta\Omega_\mu(z_l, z_s, M_{vir}, \mu_{min})\frac{dn(z_l, M_{vir})}{d\ln M_{vir}}, \quad (13)$$

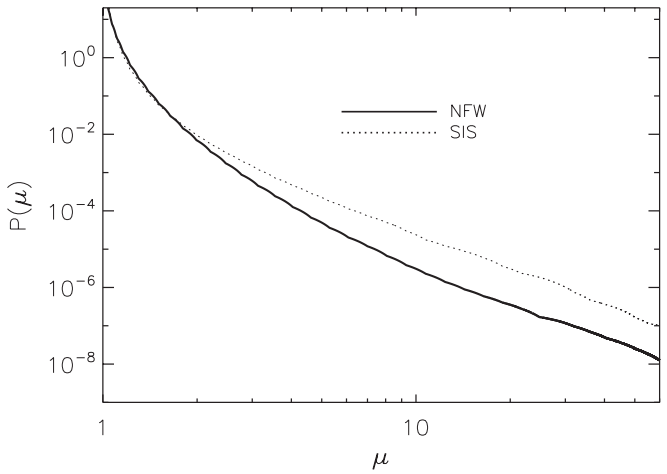

Figure 5. Magnification probability density, $P(\mu)$, for NFW and SIS mass profiles for a source at $z = 2$. At low magnifications the magnification probabilities of two profiles are comparable, but they become increasingly divergent at $\mu \gtrsim 3$, where higher magnifications are expected for the SIS model. This means that if all other parameters are fixed, the NFW model predicts fewer of the most apparently luminous sources (see also Figure 7). The curves are normalized such that the enclosed area integrates to 1, although the demagnification from weak lensing at $\mu \sim 1$ is not considered.

where $P(z_s)$ is the redshift distribution of the background SMGs, and we set $M_{\rm min} = 10^{12}\,h^{-1}\,M_\odot$ as the lower limit of the mass integral. The upper limit of the mass integral, $M_{\rm max}$, is set to $10^{15}\,h^{-1}\,M_\odot$, and therefore the effect of groups and clusters, including galaxies embedded in groups and clusters, is implicitly included in the calculations.

We use $P(z_s)$ from the model of Béthermin et al. (2011) for $S_{500} > 1$ mJy (Figure 3, bottom panel). This model, of the intrinsic HerMES SMG redshift distribution (Figure 3, bottom panel), contains faint galaxies that are mostly concentrated at $z \sim 1$, with a decreasing tail thereafter. However, we note that the details of the choice of the redshift distribution of the background sources do not significantly affect our conclusions (see also Section 4.2). While the SMG population peaks at $z \sim 1$–3, we note that the redshift distribution of lensed galaxies does not directly trace the background population since it is weighted by the optical depth to lensing, which is a function of redshift and increases in a nonlinear manner, so most of the SMGs that are lensed are expected to be at $z \sim 3$, as is observed (Figure 3).

The lensing probability (the probability of having a magnification larger than μ) is given by (Lima et al. 2010a)

$$P(>\mu) = 1 - e^{-f_\mu}, \tag{14}$$

from which we can calculate the probability distribution of magnification, $P(\mu) = -dP(>\mu)/d\mu$, for HerMES sources.

Figure 5 presents the magnification probability distribution for foreground NFW and SIS profiles lensing a source at $z = 2$. This confirms that few SMGs are strongly gravitationally lensed, and those that are magnified by factors $\gtrsim$10 are rare. As expected (see also discussion in Perrotta et al. 2002), higher magnifications are more frequent for the SIS compared to the NFW profiles. However, at lower magnifications, which are generally more likely, the SIS and NFW profiles have similar $P(\mu)$. We note that the NFW and SIS profiles do not encompass all possible galaxy mass profiles. For example, edge-on disks can significantly affect the magnification attained (Blain et al. 1999a). However, the current data are insufficient to statistically distinguish between even the simple NFW and SIS profiles (Section 4.2), and therefore further data are required to determine the distribution of mass profiles affecting strongly lensed SMGs.

Lensing magnification increases the solid angle, Ω, and the integrated flux, S, of the lensed sources by a factor of μ. The number counts of SMGs have a steep slope at bright fluxes, so lensing magnification results in an increase in the number density of sources above a fixed flux limit. By definition, the observed and intrinsic (unlensed) quantities are related by

$$S_{\rm obs} = \mu S, \tag{15}$$

$$d\Omega_{\rm obs} = \mu d\Omega. \tag{16}$$

For a given magnification the intrinsic differential number density, dn/dS, is modified as (Refregier & Loeb 1997)

$$\frac{dn}{ds} \rightarrow \frac{1}{\mu^2}\frac{dn}{dS}\bigg|_{S=S_{\rm obs}/\mu}. \tag{17}$$

Following the formalism and the discussion of Lima et al. (2010a), the observed differential number counts for a population are then

$$\frac{dn_{\rm obs}(S_{\rm obs})}{dS_{\rm obs}} = \frac{1}{\langle\mu\rangle}\int d\mu \frac{P(\mu)}{\mu}\frac{dn}{dS}\left(\frac{S_{\rm obs}}{\mu}\right), \tag{18}$$

where

$$\langle\mu\rangle = \int d\mu\, \mu P(\mu) \tag{19}$$

and the cumulative number counts are

$$n_{\rm obs}(>S_{\rm obs}) = \frac{1}{\langle\mu\rangle}\int d\mu P(\mu) n\left(>\frac{S_{\rm obs}}{\mu}\right). \tag{20}$$

The limits of these integrals are set to $\mu_{\rm min} = 2$ and $\mu_{\rm max} = 50$, as previously discussed. The maximum magnification, $\mu_{\rm max}$, is determined by the size of the background source (Peacock 1982). Perrotta et al. (2002) calculated that $\mu_{\rm max} = 10$–30 for 1–10 kpc sources at $z = 1$–4, and SMGs in lensing simulations by Serjeant (2012) are observed with $\mu \leqslant 33$, although most have $\mu < 10$. The star formation regions in SMGs are thought to be a few to 10 kpc in extent (e.g., Tacconi et al. 2006; Younger et al. 2008; Hailey-Dunsheath et al. 2010; Ferkinhoff et al. 2011), although some may be as small as ~100 pc (Swinbank et al. 2010). Furthermore, the gas reservoirs in SMGs are often more extended than the star formation (Ivison et al. 2011; Riechers et al. 2011b). Therefore, the choice of appropriate maximum magnification factor is not straightforward, and $\mu_{\rm max} = 50$ is chosen as a conservative limit. We have also considered $\mu_{\rm max} = 20$ and $\mu_{\rm max} = 30$ and find that the choice of higher $\mu_{\rm max}$ mainly affects the bright end of the predictions from the model, since high values of μ are required to lens SMGs to the brightest apparent fluxes. Thus, a lower value of $\mu_{\rm max}$ would reduce the bright end of the mean magnification in Figure 8 (top panel) and reduce the numbers of extremely bright lensed sources ($S_{500} \gtrsim 300$ mJy) such that observed sources with those flux densities are typically local late-type galaxies (top panel of Figure 10). As additional data are obtained, it is likely that $\mu_{\rm max}$ will be constrained by observational results.

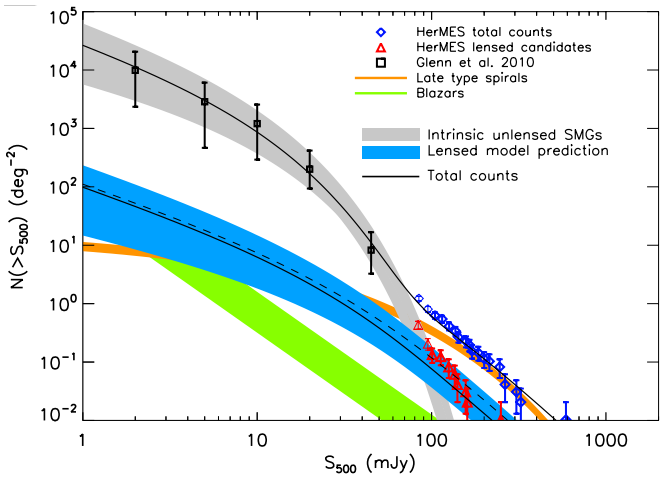

Figure 6. Cumulative 500 μm number counts for HerMES blank-field catalogs (Oliver et al. 2010) and $P(D)$ analysis (Glenn et al. 2010); the number counts of the candidate strongly gravitationally lensed sources in HerMES (Table 4) are also shown. Shaded regions represent the 68% uncertainty in the model components and prediction for the NFW lensing model. The intrinsic number counts and the contributions from blazars and local spiral galaxies are constrained by the available data. However, the number counts of the lensed sources are a prediction; in this case the shaded region captures the uncertainty in the modeled statistical lensing rate, due to a combination of uncertainties in intrinsic counts and the redshift distribution. The solid line inside the prediction is the best-fit solution for the model based on the NFW profile. The dashed line is the prediction if we instead use the SIS profile for the deflectors *and hold all other parameters fixed*. Note that when using the SIS profile and minimizing over all the available parameters the result is consistent with that for the model that utilizes the NFW profile (see Figure 7). The model prediction agrees with the data for the number of candidate lensed SMGs with $S_{500} \gtrsim 100$ mJy, but at $S_{500} \sim 80$ mJy we observe marginally more supplementary lens candidates than predicted by the model. This is consistent with the supposition that the supplementary lens candidates have a lower fidelity than the principal sample and a higher fraction that are unlensed, intrinsically luminous galaxies.

(A color version of this figure is available in the online journal.)

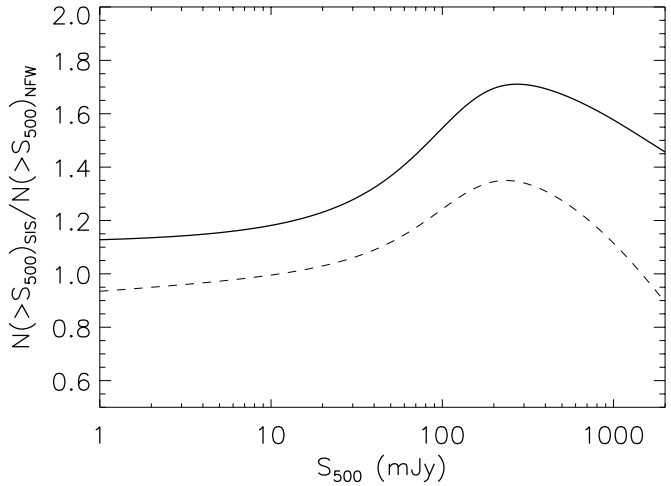

Figure 7. Ratio of the number of strongly gravitationally lensed sources predicted by the NFW and the SIS models, as a function of apparent 500 μm flux density. The solid line shows the case in which both models use the best-fit parameters from the NFW minimization and only the shape of the deflector profiles is changed. In this case the number of lensed sources predicted by the SIS profile always exceeds that from the NFW profile, although at 500 μm flux densities below ~30 mJy the differences are minimal. The difference rapidly increases for sources with $S_{500} \sim$ 30–200 mJy and above this limit peaks at $N(>S_{500})_{\rm SIS}/N(>S_{500})_{\rm NFW} \sim 1.7$ for $S_{500} \sim 200$ mJy. Note that if, instead of fixing the parameters to the values from the NFW minimization, the parameters of the SIS model are derived from fitting that model, the prediction of the number of lenses sources is comparable to that from the NFW model (dashed line).

The intrinsic number counts of SMGs are most commonly parameterized as Schechter (1976) functions or broken power laws (e.g., Coppin et al. 2006; Weiß et al. 2009b; Lindner et al. 2011). These two forms diverge only at the faint and bright ends (see, e.g., Paciga et al. 2009) and cannot be distinguished with existing data. At the bright end the broken power law has a flatter slope than the Schechter function and allows for a higher number of intrinsically luminous sources. Consequently, models with the intrinsic number counts parameterized by a broken power law predict fewer strongly lensed sources than models that make use of the Schechter function parameterization. As current data do not allow it, we do not attempt to discriminate between these models, although we note that additional constraints may be possible as studies of the brightest submillimeter sources progress (e.g., Section 6). For simplicity, we make use of a three-parameter Schechter function, characterized by a flux density, S', beyond which the distribution is steeper and gravitational lensing is more effective at boosting the observed number of sources (Schechter 1976):

$$\frac{dn(S)}{dS} = \left(\frac{N}{S'}\right)\left(\frac{S}{S'}\right)^{\alpha} e^{-S/S'}. \quad (21)$$

Here, α is the slope of the counts below the characteristic flux density, S', and N/S' is the normalization.

The model described above is fit to the HerMES 500 μm number counts (Figure 6). We run an MCMC code and calculate the χ^2 for different combinations of the Schechter distribution parameters, requiring the total 500 μm counts to fit the low flux data points (up to 45 mJy) from the $P(D)$ analysis (Glenn et al. 2010). For bright sources, the number counts presented here are consistent with the analyses of HerMES SDP data by Oliver et al. (2010) and Glenn et al. (2010), which are also shown in Figure 6.

To run the MCMC analysis, we used a modified version of the CosmoMC (Lewis & Bridle 2002) package, fixing the input cosmology to the WMAP-7 best fit from Komatsu et al. (2011). The convergence diagnostic is based on the Gelman and Rubin R statistic (Gelman & Rubin 1992). As described above, the minimum and maximum halo masses are fixed to 10^{12} and $10^{15}\,h^{-1}\,M_{\odot}$, respectively, and the minimum and maximum magnifications are set to $\mu = 2$ and 50, respectively. Thus, N, S', and α, from the Schechter function description of the intrinsic 500 μm number counts, are the only free parameters in the model.

The model is constrained by the total number counts and the numbers of blazars and local spiral galaxies. We do not attempt to constrain the intrinsic flux densities or redshift distribution of HerMES galaxies with the lensing counts. We simply show that, down to the present accuracy, and with existing models, our predicted lensing counts are consistent with the sample of HerMES candidate lensed SMGs (Section 4.2 and Figure 6). In the future, when additional data are available and the nature of a higher fraction of candidates is confirmed, it may be possible to constrain the model further.

Unless explicitly stated, all the results presented in this paper are for NFW profiles, although in Figure 7 we also consider the effect of instead using the SIS profile.

4.2. Model Predictions

We next use the statistical model of galaxy–galaxy lensing, described in Section 4.1 and constrained by the observed

HerMES 500 μm number counts, to make predictions about the prevalence and population of lensed HerMES SMGs.

In Figure 6 we show the model, the total observed number counts in HerMES blank fields, and the candidate strongly gravitationally lensed sources from Table 1. The contribution to the model from unlensed (intrinsic) SMGs, local late-type galaxies, and blazars is also shown in Figure 6. The model number counts for these three components are constrained by observational data, and the shaded regions represent the range of parameters that correspond to the 68% confidence limits. The blazars are modeled as a power law, and the local late-type galaxies as a power law with an exponential cutoff at 80 mJy, i.e., $dN/dS \propto S^{\alpha}\exp(-S_0/S)$, with $S_0 = 80$ mJy. The predicted distribution of strongly lensed SMGs is derived from an intrinsic Schechter function, using the model described in Section 4.1.

The model shown in Figure 6 corresponds to NFW mass profiles for the foreground lenses. If SIS profiles are used instead and the model parameters recalculated, we find that the prediction for the number counts of strongly lensed sources is comparable to the NFW result (Figure 7, dashed line). Hence, it appears that the choice between the two profiles is not important in fitting the current data. We investigate this conclusion further by using the SIS profile with parameters derived from the best-fit NFW model and show the resulting prediction for the counts of lensed sources in Figure 6. The ratio of the predictions from the NFW model and the SIS model with NFW parameters is shown in Figure 7.

There is minimal difference at the faintest flux densities: when the profiles are fit separately, we find that for $S_{500} \lesssim 30$ mJy the ratio $N(>S_{500})_{\rm SIS}/N(>S_{500})_{\rm NFW}$ is <1.2, and the difference between the models increases for $S_{500} \sim 30$ and 200 mJy, to a maximum of $N(>S_{500})_{\rm SIS}/N(>S_{500})_{\rm NFW} \sim 1.7$ at $S_{500} \sim 200$ mJy. The increase in the ratio at bright fluxes is expected, because the difference between the two mass profiles is most pronounced at the high-magnification end (see Figure 5). The sharp cutoff in the number of sources that are intrinsically bright means that the sources with high apparent flux densities are typically subject to larger magnification factors (see Figure 8, top panel), which is where the difference in the probability of magnification between the NFW and SIS profiles is most pronounced.

There are two underlying reasons for this behavior between NFW and SIS models. NFW models underpredict the lensing cross section at the low-mass end where baryons dramatically steepen the total mass profile. SIS models overpredict the lensing cross section at the high-mass end as the velocity dispersion is based on the virial mass and not the sub-halo mass. As shown in Figure 6, current data are unable to distinguish between the two profiles. Therefore, we refer to the NFW profile for the remainder of this paper. With additional data from follow-up programs, we may eventually be able to distinguish between different foreground mass profiles, including additional profiles that are not considered here, and provide further constraints on the models. However, as discussed by Perrotta et al. (2002), the magnification distribution is dominated by foreground deflectors with a small range of masses; therefore, such effects are expected to be negligible.

In Figure 8 (top panel), we show the prediction of the mean magnification of strongly lensed sources, which increases as a function of apparent 500 μm flux density. For sources with $S_{500} = 100$ mJy the model predicts that the mean magnification of the lensed sources is $\mu = 9.1 \pm 2.5$, where the range indicates the uncertainty in the model. For brighter sources with $S_{500} =$ 250 mJy, the calculated mean magnification is 16.9 ± 2.7. Fainter lensed SMGs, such as those in our supplementary sample ($S_{500} = 80$–100 mJy), have lower magnifications, with $\mu \sim 7$ on average, although there may be individual examples with much higher amplifications. We note that the prediction of relatively low ($\mu \lesssim 10$) flux amplifications for the majority of sources is qualitatively consistent with results from the simulated lensing of individual SMGs (Serjeant 2012).

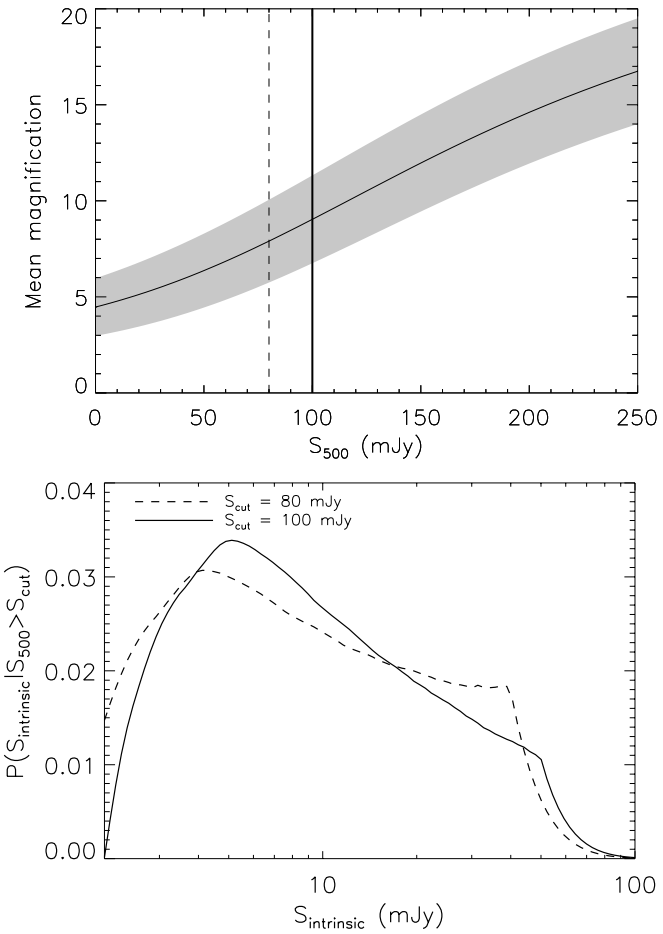

Figure 8. Top: predicted mean magnification of strongly lensed sources as a function of observed 500 μm flux density. The shaded region represents the 68% confidence limits of the model, and the solid line is the best-fit result. For sources with $S_{500} = 100$ mJy, the typical magnification is predicted to be a factor of 6–11, while for the supplementary sample, the typical magnification is only a factor of 5–9. Bottom: $P(S_{\rm intrinsic}|S_{500} > S_{\rm cut})$, the predicted distribution of the intrinsic (i.e., before lensing) 500 μm flux density of strongly gravitationally lensed SMGs selected with observed $S_{500} > 80$ or 100 mJy. The predicted intrinsic flux density distribution of the lens candidates peaks at $S_{\rm intrinsic} = 5$ mJy, and 65% of sources have $S_{\rm intrinsic} < 30$ mJy, which is the HerMES nominal detection limit at 500 μm (90% completeness; L. Wang et al. 2012, in preparation), and thus 65% of the gravitationally lensed SMGs constitute a population that would otherwise be undetectable. The strongly lensed sources in our supplementary sample ($S_{500} \geqslant 80$ mJy) are predicted to have a similar distribution of intrinsic flux densities.

Qualitatively, the trend of apparently brighter sources being more highly magnified is easy to understand, because intrinsically faint sources are more numerous than bright ones. Therefore, strongly lensed sources with observed flux densities $S_{500} \lesssim 100$ mJy may be the result of magnifying one of the numerous sources with intrinsic $S_{500} \sim 30$–50 mJy by a factor of a few. The dearth of unlensed sources with $S_{500} \sim 100$ mJy makes it less likely that the most apparently luminous sources will have low magnifications (see also Figure 9, top panel).

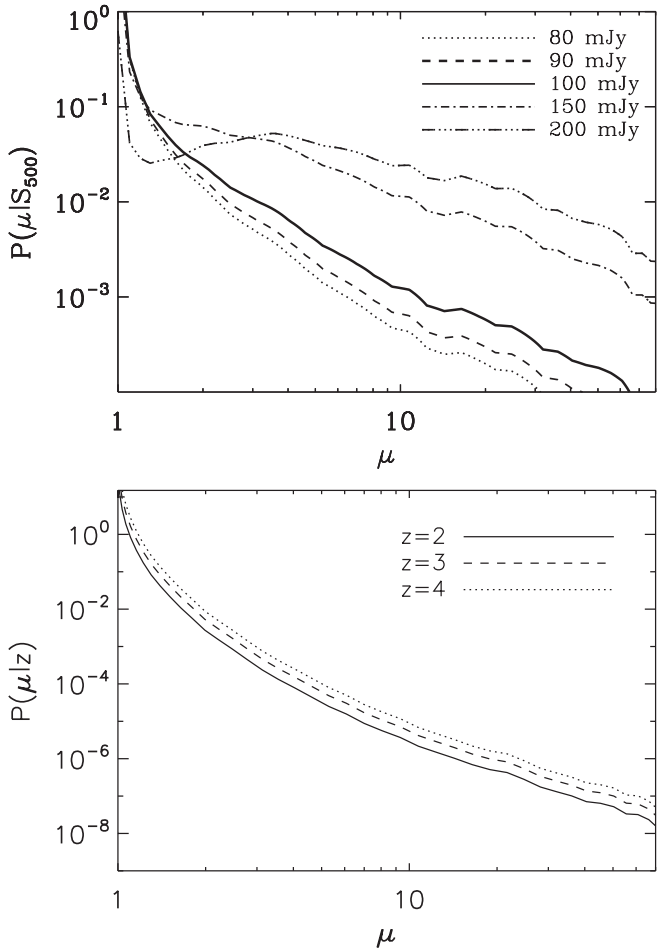

Figure 9. Top: the conditional magnification probability $P(\mu|S_{500})$, i.e., the probability of achieving a magnification, μ, given an observed flux density, S_{500}, for SMGs. The thick line shows the magnification at $S_{500} = 100$ mJy, which is the selection limit for our lensed candidates. For $S_{500} \leqslant 100$ mJy the magnification probability decreases steeply as μ increases, but for $S_{500} \geqslant 150$ mJy, the probability distribution is flatter due to the rarity of sources with intrinsic 500 μm flux densities $\gtrsim$70 mJy. Bottom: the conditional magnification probability $P(\mu|z)$, i.e., the probability of achieving a magnification, μ, given an SMG redshift, z. For $z = 2$–4 there is little dependence on redshift, demonstrating that the exact redshift distribution of the background (lensed) sources in the model has a minimal effect on the results. In both panels the demagnification from weak lensing at $\mu \sim 1$ is not considered and the curves are normalized to integrate to 1.

We also consider the predicted intrinsic (i.e., before lensing amplification) 500 μm flux density distribution of strongly lensed sources that are selected with apparent flux densities above a fixed limit ($S_{\rm cut}$). Figure 8 (bottom panel) shows that strongly lensed sources, with observed $S_{500} > 100$ mJy (such as the candidates presented here), have a broad distribution of intrinsic 500 μm flux densities, peaking at $S_{\rm intrinsic} = 5$ mJy, and 65% of sources have $S_{\rm intrinsic} < 30$ mJy. The results are similar for an observed flux density cut of 80 mJy (such as our supplementary sample). The sharp turnover in the curves that occurs at $S_{\rm intrinsic} \simeq S_{\rm cut}/2$ is caused by the combination of our definition of strong lensing ($\mu > 2$) and the steep decrease in the number counts at the bright end. The nominal HerMES detection limit is 30 mJy at 500 μm (90% completeness; L. Wang et al. 2012, in preparation), and thus ∼65% of the strongly lensed SMGs are sources that would otherwise not be detected. The amplification from gravitational lensing makes these sources ideal targets for the detailed study of high-redshift, star-forming galaxies, which would otherwise be prohibitively faint.

Within the framework of the model we can also calculate $P(\mu|S_{500})$, the probability of a source with a given observed flux density being magnified by a factor, μ, as a function of S_{500} (Figure 9). Indeed, $P(\mu|S_{500})$ provides a measure of the predicted magnification distribution for sources with a given apparent 500 μm flux. Figure 9 (top panel) shows that for $S_{500} \leqslant 100$ mJy, the probability of lensing decreases with increasing magnification and $\mu \gtrsim 10$ is rare, having a probability of $\sim 10^{-3}$, among detected galaxies. However, at the brightest flux densities, $S_{500} \geqslant 150$, the probability distribution is flatter, due to the rarity of intrinsically bright sources. Note that $\mu_{\rm max} = 50$ (Section 4.1), so for the purposes of calculating the predicted number counts we only consider the range $\mu = 2$–50.

We also investigate the effect of the background (lensed) source redshift distribution on the probability of the source being magnified by μ. Figure 9 (bottom panel) shows $P(\mu|z)$ and demonstrates that for $z = 2$–4, the assumed redshift distribution has only a small effect on our analysis. Indeed, the prediction of the model and the results presented in this paper are insensitive to the exact form of the assumed redshift distribution of SPIRE sources. We note that if we use the redshift distribution from the Valiante et al. (2009) model instead for the Béthermin et al. (2011) model, the difference in the predicted number counts, mean magnification, and lensed fractions is within the 68% confidence limits of our results.

Figure 10 shows the predicted fraction of strongly lensed sources as a function of observed 500 μm flux density. The analysis is based on our statistical model only; in Section 4.3 we show that blending is only a minor effect.

We first consider all the 500 μm sources and find that the strongly lensed fraction varies from <1% for $S_{500} < 14$ mJy to a peak of 13% at $S_{500} = 105$ mJy and then declines for the brightest fluxes (Figure 10, top panel). The decline for $S_{500} \gtrsim 100$ mJy is the result of the contribution of local late-type galaxies—at these flux densities the 500 μm population is increasingly dominated by local spirals (Figure 6). Observationally, our data contain 49 local late-type galaxies, 13 lens candidates (nine confirmed; Section 6), and no blazars with $S_{500} > 100$ mJy. Thus, 8%–23% of HerMES sources with $S_{500} > 100$ mJy are gravitationally lensed, which is in agreement with the model.

If blazars and local spirals are excluded, then the fraction of strongly lensed sources increases from <1% for $S_{500} < 15$ mJy to 100% for $S_{500} \gtrsim 200$ mJy (Figure 10, bottom panel). A correction of <1% is required for blending (Section 4.3), so these values are applicable to HerMES lensed candidates. Smaller catalog flux limits have greater contamination from unlensed SMGs. For $S_{500} \geqslant 100$ mJy 32%–74% of the sources are strongly lensed; for $S_{500} \geqslant 80$ mJy (corresponding to our supplementary sources) the strongly lensed fraction is only 14%–40%. In Section 6, we show that nine of the 13 HerMES candidates are lenses, and the nature of the remaining four is unknown (Section 6). Similarly, Negrello et al. (2010) confirmed that all five H-ATLAS $S_{500} \geqslant 100$ mJy candidates in their SDP data are gravitationally lensed. Thus, observationally, >78% of *Herschel* lensed galaxy candidates with $S_{500} \geqslant 100$ mJy are bona fide lenses. These values are consistent with the predictions from our model, although the small number of sources dominates observational uncertainties.

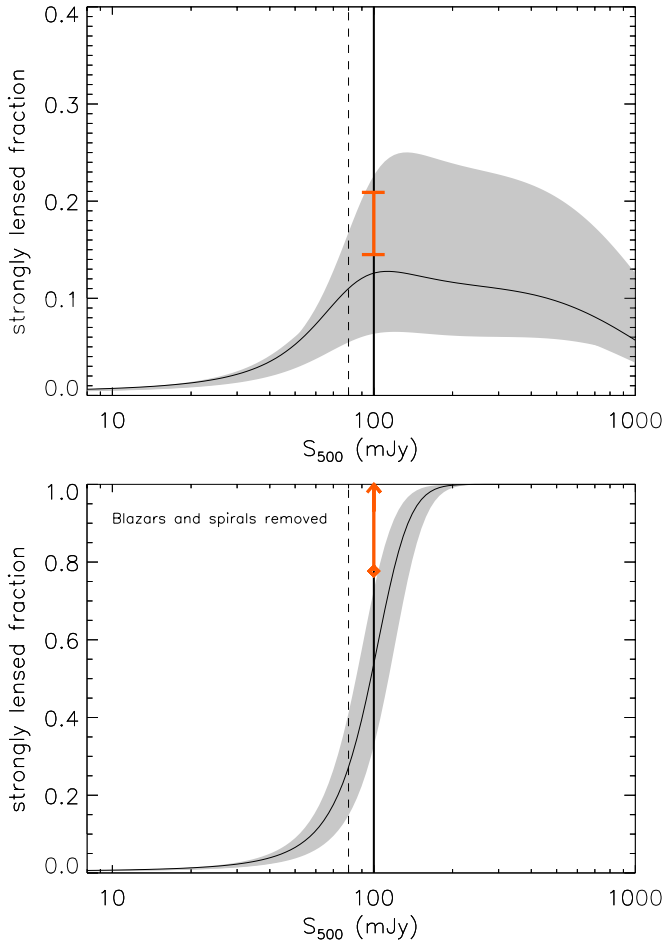

Figure 10. Predicted fraction of strongly lensed SMGs, for sources with 500 μm flux density brighter than S_{500}. Shaded regions represent the 68% confidence limits, and solid curves are the best-fit models. Solid and dashed vertical lines demarcate the selection limits of our primary and supplementary lens candidates, respectively. Top: fraction of all 500 μm sources that are predicted to be strongly lensed. The decrease at $S_{500} \gtrsim 100$ mJy is due to the increasing contribution from local late-type galaxies, which dominate the number counts at the brightest fluxes. The error bar is the observed fraction of HerMES sources with $S_{500} > 100$ mJy that are gravitationally lensed: the range is due to the four lens candidates with insufficient data to determine their nature. Bottom: fraction of 500 μm sources that are predicted to be strongly lensed, excluding local late-type galaxies or blazars. The arrow shows the fraction of the 18 *Herschel* candidates (13 in HerMES, this paper; five in H-ATLAS, Negrello et al. 2010) that are lensed. The model predicts that 32%–74% of the candidates are lensed, which is consistent with the available data. For the supplementary candidates, with $S_{500} = 80$–100 mJy the predicted lensed fraction drops to 15%–40%.

(A color version of this figure is available in the online journal.)

4.3. Could Blended Sources Contaminate Lensed SMG Selection?

Thus far, the model results presented for bright *Herschel* 500 μm sources only include individual sources and strongly lensed SMGs. It is possible that multiple faint sources could be blended in the SPIRE beam and mimic bright, gravitationally lensed SMGs. This is the same process that creates confusion noise in submillimeter data. When dealing with catalogs, it effectively shifts sources from lower to higher flux bins such that the total number of bright sources is higher than reality.

Sources that are separated by 18″ or greater are reliably deblended in the HerMES catalogs (L. Wang et al. 2012, in preparation) used here. Therefore, we consider sources that are located within 18″ of each other as blended. We use the intrinsic cumulative number counts (Figure 6) and begin by calculating the probability that two, three, or four sources of equal flux density (or greater) are located within 18″ of each other (Figure 11); in this way we are able to consider the blending rate as function of apparent (observed) flux density. We then remove the requirement for an equal flux density cutoff in the statistics and instead consider the probability that any two, three, or four sources with total flux density greater than 100 mJy are blended (Figure 12).

The cumulative intrinsic 500 μm number counts from Figure 6 are used to calculate the Poissonian probability that randomly distributed sources of equal or greater flux density are

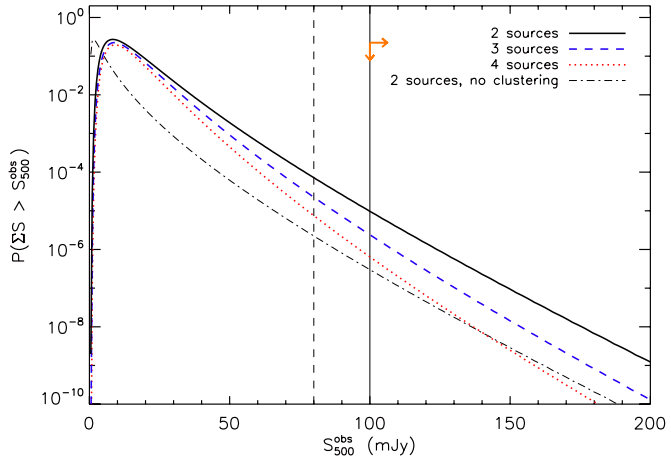

Figure 11. Probability of multiple sources blending in the *Herschel* beam and being detected as a single source with a total flux density $> S_{500}^{obs}$. The calculation uses the cumulative number counts and assumes that the minimum flux density of the components is equal. We show the results for two, three, and four blended sources, with clustering from Cooray et al. (2010a), and for two sources without clustering. Vertical solid and dashed lines represent the selection limits of our primary and supplementary lensed candidate catalogs, respectively. Arrows denote the limits obtained from follow-up observations of lens candidates, which is consistent with the model. Blending is rare in bright cataloged sources: lens candidates, with $S_{500}^{obs} \geqslant 100$ mJy, have a probability of $\sim 10^{-5}$ of being blends of multiple equi-flux sources. The number of sources in the blend only has a minor effect on the likelihood of occurrence.

(A color version of this figure is available in the online journal.)

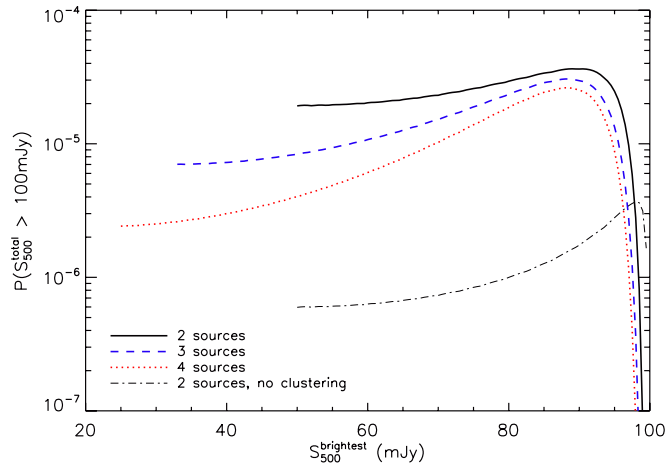

Figure 12. Probability of multiple sources, with flux densities totaling more than 100 mJy, blending in the *Herschel* beam, as a function of $S_{500}^{brightest}$, the minimum 500 μm flux density of the brightest component. Probabilities for two, three, and four sources with clustering from Cooray et al. (2010a) are shown, in addition to the unclustered, two-source case. Blending in the HerMES catalogs is unlikely to produce sources that mimic gravitationally lensed SMGs.

(A color version of this figure is available in the online journal.)

located within 18″ of each other. The effect of the clustering of SMGs is included by using $w(\theta)$ as measured for HerMES sources with $S_{500} > 30$ mJy; in this case $w(18'') = 5.7 \pm 2$ (Cooray et al. 2010a). Clustering boosts the probability of blending because the sources in a clustered distribution are more likely to reside close to other sources. Indeed, Figure 11 shows that, among sources with observed $S_{500} > 20$ mJy, blending is ∼30 times more prevalent in the clustered population.

Figure 11 shows that the probability of two 50 mJy or brighter sources being blended into a single 100 mJy or brighter source is 9.7×10^{-6}. For three or four blended sources the probabilities are 2×10^{-6} and 6×10^{-7}, respectively. At the $S_{500} \geqslant 80$ mJy corresponding to our supplementary sample of lens candidates (see the Appendix), the probability is an order of magnitude higher at the level of 7×10^{-5}. However, even in this case one in ∼14,000 of these candidates is expected to be blended, while for the brighter flux density cut of our primary sample, one in ∼100,000 is expected to be blended.

We also consider the possibility that galaxies of unequal flux densities are blended in the HerMES catalogs. Figure 12 shows the probability that two, three, or four sources with total $S_{500} \geqslant 100$ mJy are blended, as a function of the flux density of the brightest component. It is apparent from Figure 12 that the blending of intrinsically bright sources ($S_{500} \gtrsim 95$ mJy) with intrinsically faint sources is unlikely; this is due to the intrinsic rarity of such luminous sources. The probability of a >100 mJy source being a blend of any two fainter galaxies is always $<5 \times 10^{-5}$.

These results are expected since our selection limit of $S_{500} \geqslant 100$ mJy is ∼15× the *Herschel* point-source confusion noise. We note that blending contamination at a level of ≳1% contamination requires clustering of $w(18'') \gtrsim 180$—∼30× higher than that extrapolated from larger scale observations. Therefore, our results are robust to the uncertainty in the SMG clustering. We conclude that the blending of sources is rare among sources selected with $S_{500} > 100$ mJy, and none of the lens candidates presented in this paper are likely to be blends of unlensed sources.

5. FOLLOW-UP DATA

The confirmation and further study of the HerMES gravitational lens candidates require additional data. To that end, we have undertaken extensive multi-wavelength follow-up programs. Unfortunately, due to scheduling constraints and source visibility, the ancillary data coverage is non-uniform across the sample of 13 principal sources. We summarize the follow-up programs here, and in Section 6 we use the available ancillary data to investigate the individual candidates and show that at least nine of them are strongly gravitationally lensed.

5.1. High-resolution Imaging

High spatial resolution submillimeter interferometry, primarily at 880 μm, is from the Submillimeter Array (SMA). These data include multiple array configurations, from sub-compact to very extended, and the synthesized beam size ranges from ∼0.″3 to 3″ (FWHM). The data shown here were initially taken as part of a Director's Discretionary Time follow-up program of HerMES lensed sources (PI: A. Cooray) and later as part of a large multi-semester program of lensed *Herschel* sources (PI: R. S. Bussmann).

SMA observing conditions were typically very good, with low atmospheric opacity ($\tau_{225\,\mathrm{GHz}} < 0.08$) and good phase stability. Targets were typically observed for 1–3 hr (on-source), depending on weather conditions and the brightness of the target. We used track sharing to observe multiple targets in a given night and maximize *uv* coverage. All observations used an intermediate frequency coverage of 4–8 GHz and provide a total of 8 GHz bandwidth (considering both sidebands). For time-variable gain (amplitude and phase) calibration, we used the nearest quasar with $S_{880} > 0.5$ Jy (in some cases we used the average solution provided by the two nearest quasars). We typically used either the blazar 3C 279 or 3C 84 as the primary bandpass calibrator, while a planetary moon (often Titan) was used as the absolute flux calibrator. The Multichannel Image Reconstruction, Image Analysis, and Display software (Sault et al. 1995) INVERT and CLEAN tasks were used to invert the *uv* visibilities and deconvolve the dirty map, respectively. Natural weighting was typically chosen to obtain maximum sensitivity. Photometry is measured from SMA data using the CASA[44] task, IMFIT.

Two of the lensed SMG candidates were observed with the Jansky Very Large Array (JVLA; Perley et al. 2011) to obtain high-resolution radio interferometry at 1.4 and 7 GHz (Section 6). The data were taken as part of a larger follow-up program of lensed *Herschel* SMGs (program 11A-182; PI: R. Ivison) and were reduced using AIPS following the procedures described in Ivison et al. (2011), to achieve a resolution of <0.″25 (FWHM) in both cases.

We have also obtained high-resolution near-IR imaging with the Near Infrared Camera-2 (NIRC2) and laser guide star adaptive-optics (LGSAO) system on Keck-II (Wizinowich et al. 2006), or with the Wide Field Camera 3 (WFC3) on the *Hubble Space Telescope* (*HST*). The latter observations are aimed at the subset of lensed candidates for which AO observations are not feasible due to the lack of nearby bright stars for tip-tilt corrections.

The Keck-II/NIRC2 LGSAO imaging (programs C213N2L, PI: H. Fu; and U034N2L, PI: A. Cooray) uses the K_s-band filter (2.2 μm) and integration times of 40 and 60 minutes per target. The resulting 5σ point-source detection limit is ∼25.6 mag for a 0.″1 radius aperture. The estimated Strehl ratios with the LGSAO system are 15%–25% at the target positions. The images reach ∼0.″1 spatial resolution in the best cases (Figure 13). These Keck-II/NIRC2 data are reduced following the standard procedures using a customized Interactive Data Language (IDL) pipeline (see Fu et al. 2012). The image astrometry is determined relative to SDSS and *Spitzer* images, and the flux scale is calibrated with bright stars and galaxies detected in the Two Micron All Sky Survey.

The candidate lensed SMGs were observed as part of an *HST*/WFC3 cycle 19 snapshot program (PI: M. Negrello). Data were taken with the F110W filter (1.1 μm), and on-source integration times were at least 4 minutes per target. Longer integrations of 8 minutes were used for sources with red SPIRE colors ($S_{500} > S_{350}$), which indicate that they may be the highest redshift galaxies. The data were reduced with MULTIDRIZZLE,[45] to produce images with 0.″06 pixel^{-1} and spatial resolution of ∼0.″14. The typical 5σ point-source detection limit is ∼23.5 mag.

When listing the coordinates of the foreground lensing galaxy in Table 3, we make use of either *HST*/WFC3 or Keck-II/NIRC2

[44] http://casa.nrao.edu
[45] http://stsdas.stsci.edu/multidrizzle

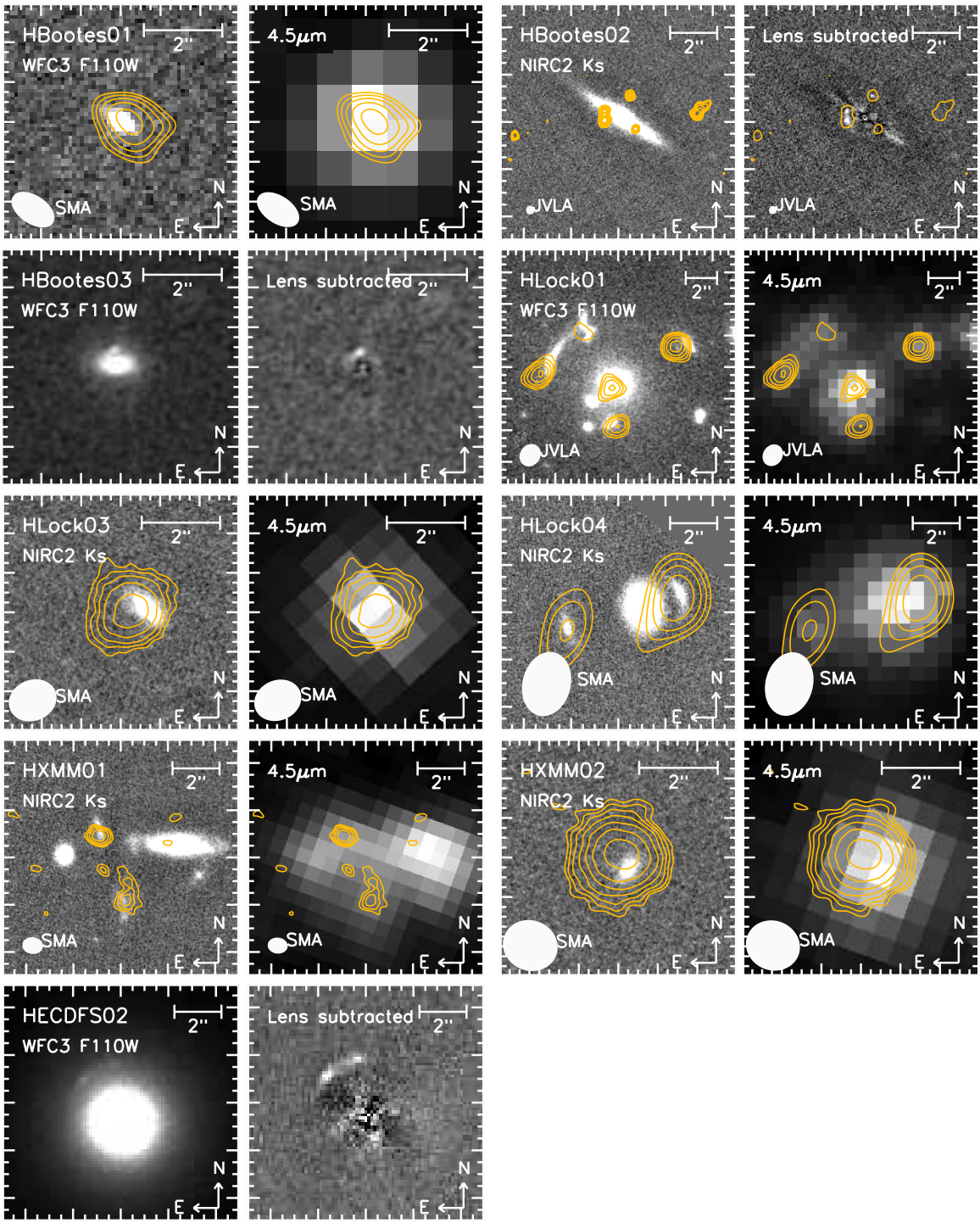

Figure 13. Images of the nine confirmed gravitationally lensed SMGs from our sample. The left-hand panels show near-IR high-resolution *HST*/WFC3 F110W or Keck-II/NIRC2 K_s-band data (as labeled). Archival *Spitzer* IRAC 4.5 μm imaging is presented in the right-hand panels. For the three cases (HBoötes02, HBoötes03, and HECDFS02) where *Spitzer* IRAC imaging is unavailable we instead show the near-IR data with the foreground lens emission subtracted in the right-hand panel. The contours on each image are submillimeter (SMA) or radio (JVLA) interferometry (as labeled). JVLA data are at 7 GHz for HBoötes02 and 1.4 GHz for HLock01. Contour levels begin at 3σ and increase by a factor of $\sqrt{2}$ at each step (expect for the right-hand panel of HBoötes01, where only the 3σ contours are shown for clarity). The contours typically trace emission from the background submillimeter source, whereas the near-IR images either are dominated by the foreground lens or contain emission from both the foreground and background sources. The exception is HLock01, in which the JVLA data trace both the lensed background SMG and radio emission in the central lensing galaxy. A 2″ scale bar is shown in the top left-hand corner of each image.

(A color version of this figure is available in the online journal.)

imaging. The locations of the background lensed SMG image components are from the SMA or JVLA data. The exact data used for the study of each lensed SMG candidate are discussed in Section 6.

5.2. Redshift Measurements

Spectroscopic redshifts of the SMGs were measured using data from multiple facilities, with the aim of observing several CO rotational transitions (e.g., Weiß et al. 2009a; Lupu et al.

Table 3
Confirmed HerMES Gravitationally Lensed Galaxies

Source	R.A.$_{\rm SMG}$[a] (J2000)	Decl.$_{\rm SMG}$[a] (J2000)	R.A.$_{\rm lens}$[b] (J2000)	Decl.$_{\rm lens}$[b] (J2000)	$z_{\rm CO}$[c]	$z_{\rm opt}$[d]	μ[e]	$\mu L_{\rm IR}$[f] ($10^{13}\,L_{\odot}$)	$T_{\rm D}$[g] (K)
HBoötes01	$14^{\rm h}33^{\rm m}30\overset{\rm s}{.}83$	$+34^{\circ}54'39\overset{''}{.}9$	$14^{\rm h}33^{\rm m}30\overset{\rm s}{.}84$	$+34^{\circ}54'40\overset{''}{.}0$	3.274	0.59 ± 0.08	$\lesssim$5 (O)	5.6 ± 0.5	41 ± 1
HBoötes02	$14^{\rm h}28^{\rm m}25\overset{\rm s}{.}54$	$+34^{\circ}55'46\overset{''}{.}9$	$14^{\rm h}28^{\rm m}25\overset{\rm s}{.}47$	$+34^{\circ}55'46\overset{''}{.}8$	2.804	0.414	$\sim$23 (R)	$3.8^{+0.4}_{-0.3}$	34 ± 1
	$14^{\rm h}28^{\rm m}25\overset{\rm s}{.}54$	$+34^{\circ}55'47\overset{''}{.}2$	...	...	...	...	...	...	...
	$14^{\rm h}28^{\rm m}25\overset{\rm s}{.}45$	$+34^{\circ}55'47\overset{''}{.}9$	...	...	...	...	...	...	...
	$14^{\rm h}28^{\rm m}25\overset{\rm s}{.}43$	$+34^{\circ}55'46\overset{''}{.}5$	...	...	...	...	...	...	...
HBoötes03[h]	$14^{\rm h}28^{\rm m}24\overset{\rm s}{.}06$	$+35^{\circ}26'19\overset{''}{.}8$	$14^{\rm h}28^{\rm m}24\overset{\rm s}{.}08$	$+35^{\circ}26'19\overset{''}{.}5$	1.325	1.034	$\lesssim$10 (O)	$1.9^{+0.3}_{-0.2}$	37 ± 1
HECDFS02	$03^{\rm h}37^{\rm m}32\overset{\rm s}{.}53$	$-29^{\circ}53'51\overset{''}{.}8$	$03^{\rm h}37^{\rm m}32\overset{\rm s}{.}40$	$-29^{\circ}53'53\overset{''}{.}6$	?	?	3.8 ± 0.02 (O)	2.6 ± 0.6	35 ± 2
	$03^{\rm h}37^{\rm m}32\overset{\rm s}{.}42$	$-29^{\circ}53'51\overset{''}{.}1$	...	...	...	...	...	...	...
HLock01	$10^{\rm h}57^{\rm m}50\overset{\rm s}{.}46$	$+57^{\circ}30'28\overset{''}{.}5$	$10^{\rm h}57^{\rm m}50\overset{\rm s}{.}96$	$+57^{\circ}30'25\overset{''}{.}7$	2.958	0.60 ± 0.04	10.9 ± 0.7 (O)	12.6 ± 0.5	51 ± 1
	$10^{\rm h}57^{\rm m}51\overset{\rm s}{.}54$	$+57^{\circ}30'26\overset{''}{.}8$	...	...	...	...	...	...	...
	$10^{\rm h}57^{\rm m}51\overset{\rm s}{.}19$	$+57^{\circ}30'29\overset{''}{.}1$	...	...	...	...	...	...	...
	$10^{\rm h}57^{\rm m}50\overset{\rm s}{.}91$	$+57^{\circ}30'23\overset{''}{.}8$	...	...	...	...	...	...	...
HLock03	$10^{\rm h}57^{\rm m}12\overset{\rm s}{.}26$	$+56^{\circ}54'58\overset{''}{.}7$	$10^{\rm h}57^{\rm m}12\overset{\rm s}{.}22$	$+56^{\circ}54'58\overset{''}{.}6$	2.771[i]	?	$3.0^{+1.3}_{-1.4}$ (O)	2.8 ± 0.2	34 ± 1
HLock04	$10^{\rm h}38^{\rm m}26\overset{\rm s}{.}60$	$+58^{\circ}15'42\overset{''}{.}6$	$10^{\rm h}38^{\rm m}26\overset{\rm s}{.}76$	$+58^{\circ}15'42\overset{''}{.}3$	?	0.58 ± 0.04	6.2 ± 0.1 (O) $5.3^{+1.3}_{-1.1}$ (D)	5.2 ± 0.6	47 ± 1
	$10^{\rm h}38^{\rm m}27\overset{\rm s}{.}19$	$+58^{\circ}15'41\overset{''}{.}3$	...	...	...	...	...	...	...
HXMM01	$02^{\rm h}20^{\rm m}16\overset{\rm s}{.}65$	$-06^{\circ}01'41\overset{''}{.}9$	$02^{\rm h}20^{\rm m}16\overset{\rm s}{.}73$	$-06^{\circ}01'42\overset{''}{.}7$	2.307	0.654/0.502[j]	$\sim$2.1[j] (O)	3.2 ± 0.3	43 ± 1
	$02^{\rm h}20^{\rm m}16\overset{\rm s}{.}58$	$-06^{\circ}01'44\overset{''}{.}3$	$02^{\rm h}20^{\rm m}16\overset{\rm s}{.}40$	$-06^{\circ}01'42\overset{''}{.}3$	...	...	$\sim$1.6[j] (O)	...	...
HXMM02	$02^{\rm h}18^{\rm m}30\overset{\rm s}{.}67$	$-05^{\circ}31'31\overset{''}{.}5$	$02^{\rm h}18^{\rm m}30\overset{\rm s}{.}69$	$-05^{\circ}31'31\overset{''}{.}9$	3.395	1.35	$1.5^{+1.0}_{-0.4}$ (O)	$3.6^{+0.3}_{-0.2}$	33 ± 1

Notes.
[a] SMG coordinates are the centroids of high-resolution submillimeter or radio interferometry, or optical arcs (as discussed in the text). Multiple coordinates are listed where there are multiple images.
[b] Coordinates of the foreground lenses are measured from optical imaging. Multiple coordinates are listed for XMM01, where there are two deflectors.
[c] $z_{\rm CO}$ is the redshift of the SMG, as traced by CO emission lines (D. Riechers et al. 2012, in preparation).
[d] $z_{\rm opt}$ is the redshift of the lens, as traced by optical spectroscopic or photometric redshifts.
[e] μ is the magnification factor from gravitational lensing. We denote the high-resolution image used to determine lensing magnification with R for radio (JVLA 7 GHz), O for rest-frame optical (Keck-II or *HST* image), or D for dust emission with SMA 880 μm.
[f] $\mu L_{\rm IR}$ is the *apparent* rest-frame 8–1000 μm infrared luminosity of the SMG.
[g] $T_{\rm D}$ is the dust temperature of the SMG, obtained by fitting an optically thin modified blackbody, with $\beta = 1.5$ to all the available 250–3000 μm photometry (Table 5).
[h] HBoötes03 was identified as lensed by Borys et al. (2006) and has been the subject of numerous additional studies (see Section 6.3).
[i] The CO redshifts of these sources are single-line redshifts guided by the submillimeter photometric redshift.
[j] The two $z_{\rm opt}$ values are for the two foreground galaxies. Furthermore, magnification factors for HXMM01 are given separately for the two lensed components as the source plane is made up of two merging SMGs (see Section 6.11).

2012; Scott et al. 2011; Riechers et al. 2011a) as the detection of at least two emission lines is required for a secure redshift determination. The data are primarily from a large program on the Combined Array for Research in Millimeter-wave Astronomy (CARMA; PI: D. Riechers), which is supplemented with observations from the Institut de Radioastronomie Millimtrique (IRAM) Plateau de Bure Interferometer (PdBI; PIs: A. Omont and D. Reichers) and the Zpectrometer spectrometer (Harris et al. 2007) on the 100 m diameter GBT (PI: A. Harris).

CO redshifts and 3 mm continuum photometry are adopted from D. Riechers et al. (2012, in preparation) and were obtained through "blind" detection of CO emission lines observed in wide-band frequency scans of the 3 mm atmospheric window with CARMA. Observations were predominantly taken in the compact D-array configuration, where the CARMA beam is 5″ FWHM. Therefore, the CARMA data are primarily used for spectral line identification and continuum photometry. Further observations were obtained at 1 cm and 2 mm with the GBT/Zpectrometer and the IRAM PdBI, which typically target additional CO transitions to confirm the CARMA redshifts.

In Table 4, we provide the CO redshifts and highlight SMGs with only a single millimeter emission line detection. This results in a degeneracy between the identification of the line transition and the redshift. In such cases we make use of photometric redshifts derived from submillimeter photometry (as described in Section 3.2) to determine the most likely line identification, assuming that it is a CO transition. This is a reasonable assumption because CO lines are the most luminous at the observed frequencies. Additional observations are required to confirm the redshifts of these sources.

Redshifts of the foreground lensing galaxies (Table 3 and Section 6) are primarily from the public SDSS database; spectroscopic measurements are used where available and photometric redshifts otherwise. In cases where SDSS data are unavailable, the foreground detector is undetected, or the photometry is blended, we have obtained redshifts from optical spectroscopy with the Low Resolution Imaging Spectrometer (LRIS) on Keck-I (PI: C. Bridge) and the Optical System for Imaging and low-Intermediate-Resolution Integrated Spectroscopy (OSIRIS) on the Gran Telescopio Canarias (GTC; PI: I. Pérez-Fournon).

5.3. Multi-band Photometry

Spitzer/MIPS 24, 70, and 160 μm flux densities of the candidate lensed SMGs are retrieved from archival data, including the *Spitzer* Wide-Area Infrared Extragalactic Survey (SWIRE; Lonsdale et al. 2003) and the *Spitzer* Deep, Wide-Field Survey (SDWFS; Ashby et al. 2009). These are listed in Table 5, in addition to 870 μm photometry from SMA interferometry (described in Section 5.1) and millimeter continuum data from

Table 4
Candidate Strongly Gravitationally Lensed SMGs in HerMES Blank Fields

	Source	S_{250} (mJy)	S_{350} (mJy)	S_{500} (mJy)	z_{CO}[a]	z_{opt}[b]
HBoötes01	1HERMES S250 J143330.8+345439	158 ± 6	191 ± 7	160 ± 33	3.274	0.59 ± 0.08
HBoötes02	1HERMES S250 J142825.5+345547	159 ± 6	196 ± 7	157 ± 33	2.804	0.414
HBoötes03	1HERMES S250 J142823.9+352619	323 ± 6	244 ± 7	140 ± 33	1.325	1.034
HECDFS01	1HERMES S250 J033141.6−295317	156 ± 6	156 ± 4	129 ± 5	...	0.222
HECDFS02	1HERMES S250 J033732.4−295352	133 ± 6	148 ± 4	122 ± 5	...	...
HECDFS03	1HERMES S250 J032443.0−282133	84 ± 6	118 ± 4	114 ± 5	...	...
HLock01	1HERMES S250 J105750.9+573026	403 ± 7	377 ± 10	249 ± 7	2.957	0.60 ± 0.04
HLock02	1HERMES S250 J104050.5+560652	53 ± 7	115 ± 10	141 ± 7	...	...
HLock03	1HERMES S250 J105712.2+565457	114 ± 7	147 ± 10	114 ± 8	2.771[c]	...
HLock04	1HERMES S250 J103826.6+581542	191 ± 7	157 ± 10	101 ± 7	...	0.61 ± 0.02
HXMM01	1HERMES S250 J022016.5−060143	180 ± 7	192 ± 8	132 ± 7	2.307	0.6545 0.5018
HXMM02	1HERMES S250 J021830.5−053124	92 ± 7	122 ± 8	113 ± 7	3.390	1.35
HXMM03	1HERMES S250 J022135.1−062617	121 ± 7	132 ± 8	110 ± 7	2.72[c]	...
	Supplementary Sample					
HADFS01	1HERMES S250 J044153.9−540350	80 ± 6	103 ± 6	93 ± 6	...	...
HADFS02	1HERMES S250 J043619.3−552425	110 ± 6	102 ± 6	87 ± 5	...	...
HBoötes04	1HERMES S250 J142650.6+332942	142 ± 6	134 ± 6	95 ± 33	...	...
HBoötes05	1HERMES S250 J144013.0+350825	162 ± 6	128 ± 6	81 ± 33	...	0.24 ± 0.05
HECDFS04	1HERMES S250 J033210.8−270535	73 ± 6	86 ± 4	85 ± 5	...	...
HECDFS05	1HERMES S250 J032636.3−270044	155 ± 6	132 ± 4	85 ± 7	...	...
HECDFS06	1HERMES S250 J032603.3−291803	90 ± 6	56 ± 4	82 ± 5	...	...
HEGS01	1HERMES S250 J142201.4+533213	74 ± 6	99 ± 5	90 ± 6	...	0.53 ± 0.24
HELAISS01	1HERMES S250 J002906.2−421419	129 ± 6	116 ± 5	81 ± 6	...	...
HFLS01	1HERMES S250 J172612.0+583742	108 ± 7	124 ± 6	99 ± 7	...	...
HFLS02	1HERMES S250 J171450.8+592633	164 ± 7	1484 ± 6	87 ± 6	...	0.56 ± 0.02
HFLS03	1HERMES S250 J170607.7+590921	98 ± 7	106 ± 6	81 ± 6	...	0.16 ± 0.17
HLock05[d]	1HERMES S250 J103618.3+585456	71 ± 7	102 ± 10	99 ± 8	3.520[c]	0.49 ± 0.12
HLock06	1HERMES S250 J104549.2+574511	136 ± 7	128 ± 10	97 ± 9	2.991[c]	0.20 ± 0.02
HLock07	1HERMES S250 J105007.4+571653	96 ± 7	104 ± 10	87 ± 8	...	...
HLock08	1HERMES S250 J105551.2+592845	142 ± 7	119 ± 10	85 ± 8	1.699[c]	0.38 ± 0.11
HLock09	1HERMES S250 J105311.0+564205	50 ± 7	76 ± 10	82 ± 8	...	0.14 ± 0.02
HLock10	1HERMES S250 J103217.6+583113	90 ± 7	98 ± 10	81 ± 8	...	...
HLock11	1HERMES S250 J104140.3+570857	98 ± 7	113 ± 10	81 ± 8	...	0.49 ± 0.12
HXMM04	1HERMES S250 J022021.7−015328	144 ± 7	137 ± 8	94 ± 11	...	0.21 ± 0.14
HXMM05[d]	1HERMES S250 J022547.8−041750	106 ± 7	119 ± 8	92 ± 7	2.985	...
HXMM06	1HERMES S250 J021433.0−041823	93 ± 7	108 ± 8	87 ± 7	...	...
HXMM07	1HERMES S250 J021918.4−031051	91 ± 7	104 ± 8	86 ± 7	...	0.42 ± 0.07
HXMM08	1HERMES S250 J022626.1−061722	68 ± 7	77 ± 8	85 ± 7	...	...
HXMM09	1HERMES S250 J022029.2−064845	127 ± 7	115 ± 8	84 ± 7	...	0.21 ± 0.09
HXMM10	1HERMES S250 J023146.5−035132	142 ± 7	122 ± 8	83 ± 7	...	0.57 ± 0.07
HXMM11[d]	1HERMES S250 J022201.6−033340	107 ± 7	108 ± 8	81 ± 7	2.179	...
HXMM12[d]	1HERMES S250 J023006.0−034152	102 ± 7	110 ± 8	81 ± 7	...	...
HXMM13	1HERMES S250 J022141.4−070321	76 ± 7	91 ± 8	81 ± 7	...	0.38 ± 0.08

Notes. The primary source sample has $S_{500} > 100$ mJy and is expected to contain 0–5 interlopers (Section 4.2); these sources are discussed in detail in Section 6. The supplementary sample consists of fainter sources ($S_{500} = 80$–100 mJy) and is therefore less reliable.
[a] Redshift of the submillimeter source, measured from the rotational transitions of CO (D. Riechers et al. 2012, in preparation).
[b] Optical redshift, which typically traces the foreground lens.
[c] These source redshifts are measured from a single CO emission line and are guided by the submillimeter photometric redshift.
[d] The galaxies are discussed in further detail in the Appendix.

spectroscopic surveys (Section 5.2). The 2 and 2.3 mm flux densities are extracted from our PdBI data, and CARMA provides the 3 mm data. Previous studies (Conley et al. 2011; Ikarashi et al. 2011) published Caltech Submillimeter Observatory/Z-Spec 1 mm continuum flux densities for two sources (HXMM02 and HLock01), so these are also included in Table 5.

We also present 1.2 mm flux densities from the Max-Planck Millimetre Bolometer (MAMBO) instrument on the IRAM 30 m telescope (collaboration led by A. Omont and I. Pérez-Fournon). The observations are reduced and analyzed using the method described in Omont et al. (2003). The MAMBO beam is 10.″6 (FWHM) at 1.2 mm; therefore, these data cannot be used for resolved studies, since fully sampled maps were not obtained.

6. INDIVIDUAL LENS CANDIDATES

We next discuss the 13 candidate lensed SMGs identified in Section 2. Nine of these sources are shown to be gravitationally lensed. Three of these sources, HBoötes03 (Borys et al. 2006),

Table 5
Multiwavelength far-IR and Radio Photometry of Candidate Strongly Gravitationally Lensed SMGs in HerMES

	$S_{24\,\mu m}$ (mJy)	$S_{70\,\mu m}$ (mJy)	$S_{160\,\mu m}$ (mJy)	$S_{870\,\mu m}$ (mJy)	$S_{1\,mm}$ (mJy)	$S_{1.2\,mm}$ (mJy)	$S_{2\,mm}$ (mJy)	$S_{2.3\,mm}$ (mJy)	$S_{3\,mm}$ (mJy)	$S_{1.4\,GHz}$ (mJy)
HBoötes01	0.20 ± 0.01	5.69 ± 0.31	54.2 ± 1.2	61.0 ± 3.0	...	26.8 ± 1.5	...	...	0.72 ± 0.14	0.26 ± 0.04
HBoötes02	0.60 ± 0.01	9.16 ± 0.29	53.9 ± 1.2	...	...	22.4 ± 1.0	...	...	1.37 ± 0.22	11.7 ± 0.5
HBoötes03	0.28 ± 0.01	23.1 ± 0.30	142.3 ± 1.31	18.4 ± 2.5	...	9.9 ± 5.8	...	...	...	0.73 ± 0.05
HECDFS01	0.58 ± 0.02	...	...	...	...	...	...	...	...	...
HLock01[a]	1.24 ± 0.02	16.1 ± 0.24	244.4 ± 1.39	52.8 ± 0.6	27.5 ± 0.6	...	...	...	0.85 ± 0.25[a]	...
HLock03	0.25 ± 0.01	3.86 ± 0.24	69.6 ± 1.22	47.0 ± 1.3	...	17.1 ± 1.6	...	...	0.78 ± 0.11	...
HLock04	0.44 ± 0.01	3.25 ± 0.23	104.6 ± 1.27	32.1 ± 1.5	...	9.5 ± 0.9	...	...	0.34 ± 0.11	...
HXMM01	0.57 ± 0.02	17.9 ± 0.03	88.3 ± 1.04	25.1 ± 1.1	...	11.1 ± 0.9	1.1 ± 0.3	0.55 ± 0.1	...	...
HXMM02	0.12 ± 0.01	4.79 ± 0.26	31.1 ± 1.14	72.6 ± 2.2	51.9 ± 1.2	31.3 ± 0.8	...	2.23 ± 0.5	...	1.2 ± 0.5
Supplementary Sample										
HADFS01	0.81 ± 0.06	2.97 ± 0.64	...	...	...	...	...	...	...	...
HBoötes04	0.37 ± 0.01	6.84 ± 0.22	57.9 ± 1.2	...	...	...	...	...	...	11.4 ± 0.5
HECDFS04	0.15 ± 0.01	3.49 ± 0.23	23.2 ± 1.3	...	...	...	...	...	...	...
HECDFS05	...	...	...	...	...	...	...	...	...	1.2 ± 0.3
HEGS01	0.40 ± 0.01	...	...	...	...	...	...	...	...	...
HFLS01	0.88 ± 0.06	5.38 ± 0.4	...	...	...	...	...	...	...	1.8 ± 0.5
HFLS02	1.05 ± 0.06	7.13 ± 0.46	...	...	...	...	...	...	...	...
HFLS03	...	...	...	...	...	...	...	...	...	0.8 ± 0.5
HLock05[b]	0.31 ± 0.01	6.36 ± 0.23	67.0 ± 1.23	26.9 ± 0.93	...	11.3 ± 0.9	...	...	0.56 ± 0.11	...
HLock06	0.66 ± 0.02	22.6 ± 0.25	130.0 ± 1.30	...	...	...	...	...	0.57 ± 0.15	...
HLock07	0.25 ± 0.01	...	54.8 ± 1.23	...	...	5.4 ± 0.8	...	...	...	...
HLock08	...	35.6 ± 0.32	...	...	...	...	...	...	...	...
HLock11	0.26 ± 0.01	6.02 ± 0.24	41.3 ± 1.25	...	...	...	...	...	...	...
HXMM05[b]	0.37 ± 0.01	3.85 ± 0.29	...	21 ± 1.0	...	8.9 ± 0.9	0.9 ± 0.3	0.52 ± 0.4	...	...
HXMM07	0.46 ± 0.01	4.60 ± 0.23	28.85 ± 0.99	...	...	...	...	...	...	...
HXMM09	...	...	...	...	...	...	...	...	...	1.0 ± 0.4
HXMM11[b]	0.39 ± 0.01	5.22 ± 0.23	66.2 ± 1.03	18 ± 1.0	...	...	0.8 ± 0.3	...	...	...
HXMM12[b]	...	...	...	20 ± 1.0	...	...	...	...	...	7.4 ± 0.5

Notes. The primary source sample has $S_{500} > 100$ mJy and is expected to contain 0–5 interlopers; these sources are discussed in detail in Section 6. The supplementary sample consists of fainter sources ($S_{500} = 80$–100 mJy) and is therefore less reliable. Sources that are unobserved or undetected at all of these wavelengths are not included in this table.

[a] The flux for HLock01 is at 3.4 mm, not 3 mm as for the other sources.

[b] Theses sources are discussed in further detail in the Appendix.

HLock01 (Conley et al. 2011), and HXMM02 (Ikarashi et al. 2011), have been discussed previously. The four other sources require additional observations before their lensing nature can be confirmed.

Optical and infrared imaging of eight of the nine confirmed lenses is presented in Figure 13; the final source not shown here—HBoötes03—has been discussed extensively in the literature (Borys et al. 2006; Desai et al. 2006; Iono et al. 2006a, 2006b; Swinbank et al. 2006; Sturm et al. 2010; Hailey-Dunsheath et al. 2010), with multi-wavelength imaging available in several of these papers. The far-IR SEDs of all 13 candidates are displayed in Figure 14, with photometry from HerMES, our follow-up programs, and archival studies.

The basic properties of the nine confirmed lens systems are summarized in Table 3. This includes the lensing magnification factor, μ, determined from modeling the best available data. The lens modeling is performed following the procedure outlined in Section 2.2 of Gavazzi et al. (2011); we use the code SL_FIT, which has been previously used to study galaxy-scale strong lensing (Gavazzi et al. 2007, 2008). The foreground lensing potential is modeled as a cored isothermal ellipsoid. For simplicity in the modeling and to avoid computational costs associated with pixelized inversion techniques (Warren & Dye 2003; Treu & Koopmans 2004; Suyu et al. 2006), we make use of an analytical description of the source plane light distribution by assuming a Gaussian radial profile with elliptical shape (e.g., Marshall et al. 2007; Bolton et al. 2008b). Fitting is performed by minimizing the difference between the model and the data; free parameters include the shape of the background SMG and the foreground mass profile.

Due to the potential for differential magnification (e.g., Gavazzi et al. 2011; Fu et al. 2012; Hezaveh et al. 2012; Serjeant 2012), we note that these magnification estimates are only valid for the wavelength at which they are derived. Systems in which differential magnification could be important, as well as one case where modeling at both 2.2 and 880 μm shows that differential magnification is limited, are highlighted below.

Two of the lens systems presented here (HLock01, Section 6.7, Gavazzi et al. 2011; and HXMM01, Section 6.11, H. Fu et al. 2012, in preparation) have complex potentials with multiple deflectors. The primary focus of this paper is broad statistics, and therefore we do not present individual lens models or detailed properties of the foreground lensing galaxy or galaxies here. Such details, including analysis of the foreground lensing galaxies associated with *Herschel* SMGs, will be presented elsewhere (R. Gavazzi et al. 2012, in preparation). Here, we summarize the basic properties of the nine confirmed lens systems, focusing primarily on the background SMGs. Five of the candidates from the supplementary sample are described in the Appendix.

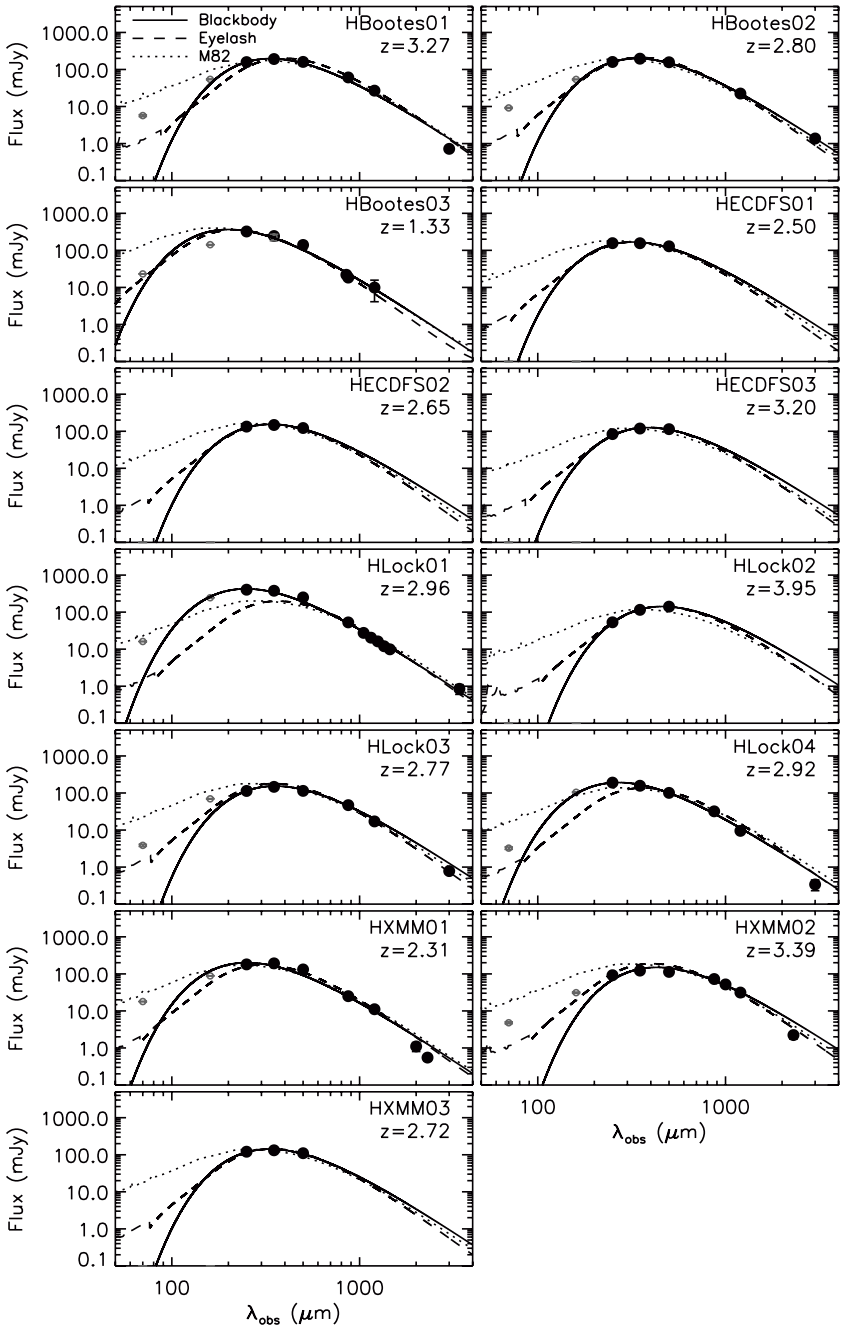

Figure 14. Observed-frame far-IR SEDs of the 13 HerMES candidate gravitationally lensed SMGs. Photometry from multiple components is integrated, such that the total flux densities are presented for each source. We show the best-fit optically thin modified blackbody SEDs, with fixed $\beta = 1.5$, corresponding to the far-IR luminosities and temperatures presented in Table 3. The SEDs of M82 (Silva et al. 1998) and the "Cosmic Eyelash" (SMM J2135−0102; Ivison et al. 2010b; Swinbank et al. 2010) are redshifted and rescaled to the observed photometry and shown for comparison. We also show 70 and 160 μm photometry from archival *Spitzer* MIPS surveys, and SHARC-II 350 μm observations of HBoötes03 (Borys et al. 2006), although these data are not used in the fitting.

6.1. HBoötes01

HBoötes01 is the second brightest 500 μm source in our sample, with $S_{500} = 160 \pm 33$ mJy. It is a confirmed gravitationally lensed SMG and has a far-IR SED similar to M82, with $T_{\rm D} \sim 40$ K for fixed $\beta = 1.5$ and $\mu L_{\rm IR} \sim 6 \times 10^{13}\,L_{\odot}$ (Figure 14; Table 3). SMA observations in the extended and compact array configurations detect a single bright source, with $S_{870} = 61 \pm 3$ mJy. HBoötes01 has a 1.4 GHz flux density of 0.26 ± 0.04 mJy (de Vries et al. 2002), which is consistent with that expected from star formation, as calculated from the far-IR/radio correlation with the method described in Section 2.

Figure 13 shows SMA contours on *HST*/WFC3 F110W imaging and SDWFS 4.5 μm images. The submillimeter emission is slightly offset from a source in the *HST* data and coincident with an IRAC source. The *HST* source is also detected in the NOAO Deep Wide-Field Survey (NDWFS) (Jannuzi & Dey 1999) and SDSS. It is red in the optical and has $r = 21.71$ mag and $z_{\rm phot} = 0.59 \pm 0.08$ in SDSS. CO($J = 3 \rightarrow 2$) and CO($J = 4 \rightarrow 3$) are detected in our CARMA data, placing the submillimeter source at $z = 3.274$. Therefore, it is clear that the optical and near-IR emission and the submillimeter emission are dominated by two distinct sources at different redshifts. Despite the existence of two sources at different redshifts and

the offset between the near-IR and far-IR emission, there are no arcs or other morphological indications of gravitational lensing in the SMA data. Therefore, the amplification from lensing is expected to be small: $\mu \lesssim 5$.

The configuration of HBoötes01 is similar to HXMM02 (Section 6.12; Ikarashi et al. 2011) and HLSJ091828.6+514223 (Combes et al. 2012). All three galaxies are gravitationally lensed, as determined from redshift information, and have small ($\lesssim$1″) offsets between the submillimeter and optical sources. However, despite high-resolution submillimeter interferometry, there are no morphological indications of lensing, and we are unable to determine the precise lensing magnification.

6.2. HBoötes02

In the HerMES SPIRE data, HBoötes02 is photometrically similar to HBoötes01, with $S_{500} = 157 \pm 33$ mJy and an SED that peaks in the 350 μm band. A single emission line is detected in CARMA observations, which is confirmed to be CO($J = 3 \rightarrow 2$) at $z = 2.804$ with the detection of CO($J = 1 \rightarrow 0$) by the GBT. SED fitting of the far-IR data shows that HBoötes02 has $T_{\rm D} = 34 \pm 1$ K and $\mu L_{\rm IR} = 3.8^{+0.4}_{-0.3} \times 10^{12}\ L_{\odot}$, for fixed $\beta = 1.5$ (Table 3 and Figure 14).

Optical data reveal that HBoötes02 is gravitationally lensed by the central region of an edge-on disk galaxy at $z = 0.414$ (Figure 13), which, due to the presence of a dust lane and its inclination angle, most likely has a higher mass density than would be estimated from its optical magnitude. The redshift of the deflector is determined from multiple emission and absorption lines observed in long-slit spectroscopy with OSIRIS on the GTC. We have also obtained a JVLA 7 GHz map of HBoötes02, which reveals four images of the background source, which are created due to gravitational lensing distortion. The images are not resolved in the 0.″25 JVLA beam, and the total flux density is 2.3 ± 0.2 mJy at 7 GHz.

Lens modeling of the radio data indicates that the system has an Einstein radius of $0.''80 \pm 0.''04$ and is magnified by $\mu_{\rm JVLA} \sim 23$ at 7 GHz. Thus, HBoötes02 is the most highly magnified source in our sample. The large magnification is due to the small size of the radio emission region, which is $\leqslant$0.″008 ($\leqslant$65 pc at $z = 2.8$) in the source plane. Since the brightness temperature is much greater than 10^4 K, these data show that an AGN is powering the radio emission.

HBoötes02 is also detected with a flux density of 12.36 ± 0.50 mJy at 1.4 GHz (de Vries et al. 2002), although its components are unresolved in those data. The observed radio spectral index between 1.4 and 7 GHz is $\alpha = -1.04$. For $\alpha = -1.04$ the expected flux density from star formation is only ~0.07 mJy and ~0.01 mJy at 1.4 and 7 GHz, respectively (based on the far-IR/radio correlation; Section 2). Therefore, the bright radio flux densities in HBoötes02 confirm that an AGN dominates the emission at these wavelengths.

HBoötes02 has also been observed with the SMA at 870 μm in extended and compact array configurations, resulting in a map with a beam of ~0.″7, in which a partial ring structure is resolved. Accounting for the larger SMA beam, the submillimeter emission appears to be more extended than the radio emission, and the flux ratios between the components differ between the two data sets. This suggests that differential lensing is important in HBoötes02 and that the submillimeter data trace the star formation and the radio data trace the AGN. Indeed, lens modeling of the SMA data determines that the submillimeter emission from HBoötes02 has $\mu_{\rm SMA} = 10.1 \pm 1.6$ and a half-light radius of $0.''15 \pm 0.''03$ (1.2 ± 0.2 kpc at $z = 2.8$). Note that the submillimeter magnification (derived from the SMA data) is significantly lower than that at radio wavelengths (from the JVLA data), which is indicative of differential lensing resulting from two different emission regions.

HBoötes02 is also point-like in Keck K-band data, which indicates that the AGN may also be dominating the near-IR emission from HBoötes02. However, lens modeling is not performed on those data because the foreground deflector contains a complex dust lane. A more reliable analysis is available from the JVLA and SMA data, which are not complicated by the dust lane in the foreground galaxy. We note that the best-fit lens models based on the radio and SMA data require deflectors with a single isothermal ellipsoid profile and high ellipticity, as indicated by the near-IR imaging. A detailed analysis of the multi-wavelength observations of HBoötes02 will be presented in J. L. Wardlow et al. (2012, in preparation).

We note that there are two additional sources detected in the JVLA data, approximately 3″ and 5″ west and east of the center of the lensing galaxy, respectively. Both of these sources are resolved, although they are not detected in optical or near-IR imaging, so their nature is unclear. It is possible that they are relic jets from HBoötes02.

6.3. HBoötes03

HBoötes03, also known as MIPS J142824.0+352619, is a gravitationally lensed source that was discovered in *Spitzer* MIPS imaging of the Boötes field (Borys et al. 2006). It has been subject to extensive analysis and follow-up observations, including broadband submillimeter photometry from SHARC-II (350 μm), SCUBA (850 μm; Borys et al. 2006), and SMA (890 μm) with 2.″5 resolution (Iono et al. 2006a). Optical, near-IR, and mid-IR spectroscopy revealed the presence of a background infrared source at $z = 1.325$ and a foreground optical galaxy at $z = 1.034$ (Desai et al. 2006; Borys et al. 2006). These data confirmed the nature of HBoötes03 as a gravitationally lensed starburst galaxy, and the existing data are consistent with our new HerMES SPIRE photometry (see Figure 14). We have fit the new SPIRE and existing submillimeter photometry with an optically thin modified blackbody with fixed $\beta = 1.5$ to yield $T_D = 41 \pm 1$ K and $\mu L_{\rm IR} = (5.6 \pm 0.5) \times 10^{13}\ L_{\odot}$.

Spitzer IRS spectroscopy shows that the mid-IR emission is dominated by star formation, with no evidence for an AGN (Desai et al. 2006). There are no morphological indicators of lensing in the submillimeter or radio data, and Borys et al. (2006) used size arguments and positional offsets between the radio/submillimeter and optical sources to estimate that the lensing magnification $\mu \lesssim 10$. We have since obtained *HST*/WFC3 F110W imaging of HBoötes03, in which a second, faint, near-IR source is present (Figure 13). This second source is ~0.″4 to the north of the $z = 1.325$ galaxy, and its position is consistent with it being the background SMG. The small separation between these sources, the point-like nature of the second source, and the absence of counter-images further support the hypothesis that HBoötes03 is only magnified by a small factor. near-IR integral field spectroscopy of the Hα emission does not contain AGN signatures and shows that the emission is spatially extended, although similar effects are not observed in H- or K-band continuum data (Swinbank et al. 2006). On the basis of the IFU data, Swinbank et al. (2006) argue that it is possible that HBoötes03 has $\mu \gg 10$ for rest-frame optical emission, although the requisite precise alignment of the system makes this unlikely.

Numerous far-IR and submillimeter emission lines have been detected in HBoötes03, including CO($J = 2\rightarrow1$) and CO($J = 3\rightarrow2$) (Iono et al. 2006b). The CO($J = 2\rightarrow1$) emission is not spatially extended in the 1.″3 beam, which Iono et al. (2006b) use to argue that $\mu \lesssim 8$ for the gas-emitting region. Recently, the [C II] 158 μm fine-structure transition was detected (Hailey-Dunsheath et al. 2010; Stacey et al. 2010), and [O I] 63 μm and [O III] 52 μm were observed with *Herschel* PACS (Sturm et al. 2010). The emission-line ratios in HBoötes03 are similar to those observed in the nuclei of local starburst galaxies, indicating that HBoötes03 may be a high-redshift, high-luminosity analog of those galaxies (Hailey-Dunsheath et al. 2010; Sturm et al. 2010).

6.4. HECDFS01

HECDFS01 is near the edge of the HerMES area, which means that it is located outside of the main ECDFS field in a region without deep data. It has not yet been observed by any of our follow-up programs, and as such the only available data are from HerMES and shallow, all-sky surveys. Therefore, we are unable to confirm whether HECDFS01 is indeed a gravitationally lensed SMG. The SPIRE colors are flat, giving a submillimeter photometric redshift of $z \sim 2.50$, although this is not well constrained. We note that the galaxy 2dFGRS S401Z151 at $z = 0.222$ is only 32″ from the SPIRE centroid, although we cannot confirm whether it is related to the submillimeter emission.

6.5. HECDFS02

HECDFS02, like HECDFS01, is in a region without deep archival data. However, follow-up imaging with *HST*/WFC3 in the F110W filter reveals gravitational arcs around a bright galaxy (Figure 13). The SPIRE fluxes of HECDFS02 peak in the 350 μm band, which indicates that it is at $z \sim 2.65$. Due to the position of HECDFS02 outside of the main ECDFS area, there is inefficient data to determine a photometric redshift for the foreground lens. However, we have used the Kormendy (1977) relation for the *J* band (de Vries et al. 2000) to estimate that the lensing galaxy is at $z \sim 0.1$. The Einstein radius is $1\farcs678 \pm 0\farcs003$, and modeling of the *HST* data shows two emitters in the source plane, which may be two star-forming regions in a single SMG or may be a merger or interaction of two galaxies. The amplification from lensing is $\mu_{\rm F110W} = 3.79 \pm 0.02$ at 1.1 μm. However, differential lensing may be important, so this value may not apply to the submillimeter data.

6.6. HECDFS03

HECDFS03 is also outside the deep survey fields, and the only follow-up data available are F110W *HST*/WFC3 imaging from our snapshot program. There are no arcs or other lensing features in the *HST* data, and although the structure of the detected sources appears to resemble a group or small cluster, we cannot verify whether HECDFS03 is gravitationally lensed. The SPIRE colors of HECDFS03 indicate that the submillimeter emission originates at $z \sim 3.20$.

6.7. HLock01

HLock01 is the brightest gravitationally lensed HerMES source, with 250, 350, and 500 μm flux densities of 403 ± 7, 377 ± 10, and 249 ± 7 mJy, respectively (Table 4). Due to its extreme brightness, HLock01 was subject to a significant follow-up effort, and it was the first confirmed HerMES lensed SMG (Conley et al. 2011). 880 μm SMA interferometry resolved the SPIRE source into four components (Conley et al. 2011), which were further resolved in Keck-II/NIRC2 *K*-band imaging. The redshift of HLock01 was established from CO emission lines as $z = 2.958$ (Scott et al. 2011; Riechers et al. 2011a), and Gavazzi et al. (2011) used the NIRC2 *K*-band data to show that the rest-frame optical emission is magnified by a factor of $\mu = 10.9 \pm 0.7$ by a small group at $z \sim 0.6$. The central group galaxy has a photometric redshift of 0.60 ± 0.04 (Oyaizu et al. 2008); photometric or spectroscopic redshifts are unavailable for the remaining group members due to their faintness. Instead, the group nature of the deflector is confirmed by the Einstein radius, $R_{\rm Ein} = 4\farcs10 \pm 0\farcs02$, corresponding to a velocity dispersion $\sigma_v = 483 \pm 16$ km s^{-1} (Gavazzi et al. 2011).

Thorough SED fitting of HLock01 was performed by Conley et al. (2011), who find that it contains optically thick warm dust, with $T_{\rm D} = 88 \pm 3$ K for $\beta = 1.95 \pm 0.14$ (note that for consistency with the rest of our sample Table 3 gives $T_{\rm D}$ for an optically thin modified blackbody with $\beta = 1.5$). Scott et al. (2011) analyzed the CO spectral line energy distribution of HLock01, including observations of the $J = 1\rightarrow0$, $3\rightarrow2$, $5\rightarrow4$, $7\rightarrow6$, $8\rightarrow7$, $9\rightarrow8$, and $10\rightarrow9$ transitions. They found that a single warm, moderate-density gas model adequately describes the data, although a second denser component may also be present. Finally, Riechers et al. (2011a) examined the dynamics of the gas in HLock01, by studying the resolved CO lines. They showed that the CO($J = 5\rightarrow4$) emission exhibits resolved velocity structure, consistent with HLock01 being a gas-rich merger at $z \sim 3$.

Since the publications of Conley et al. (2011), Gavazzi et al. (2011), Scott et al. (2011), and Riechers et al. (2011a), we have obtained *HST* WFC3 F110W and JVLA 1.4 GHz observations of HLock01, which are shown in Figure 13. The radio data have $\sim1\farcs1$ resolution and isolate the four lensed images of HLock01 with higher accuracy than the existing SMA data (Conley et al. 2011), and they show that the central lensing galaxy is also radio-bright. The total flux density in the four radio images of HLock01 is 0.97 ± 0.05 mJy, which is $\sim$4 times higher than expected from the far-IR/radio correlation, if $q_{\rm IR} = 2.40$ (Ivison et al. 2010a; see Section 2 for details). Indeed, HLock01 requires $q_{\rm IR} = 1.8 \pm 0.4$ if both the far-IR emission and the radio emission are powered by star formation. The luminous radio emission from HLock01, coupled with its warm dust temperature ($T_{\rm D} = 88.0 \pm 2.9$ K; Conley et al. 2011), suggests that HLock01 harbors both AGNs and star formation activity.

The JVLA data also reveal a radio source $\sim$75″ north of HLock01, which is composed of two bent lobes, indicative of an FR II source. Since bent FR II sources are most likely to be located in galaxy groups and clusters (e.g., Stocke 1979), this observation adds weight to the analysis of Gavazzi et al. (2011) that the foreground lens is a small group or cluster of galaxies.

6.8. HLock02

We have obtained *HST*/WFC3 F110W imaging of HLock02. No lensing features are apparent in the data, and we do not have submillimeter or radio interferometry to precisely pinpoint the source of the submillimeter emission. HLock02 has red SPIRE colors, indicative of a source at $z \sim 4$ (Figure 14), so the absence of lensing features in the WFC3 image may be because the SMG is below the detection threshold of these data. Therefore,

we cannot determine whether or not HLock02 is gravitationally lensed.

6.9. HLock03

HLock03 has $S_{500} = 114 \pm 8$ mJy with submillimeter emission peaking in the SPIRE 350 μm band. Continuum emission is detected with the SMA at 890 μm, MAMBO at 1.2 mm, and CARMA at 3mm (Figure 14). A single emission line is detected in CARMA spectroscopy, which, on the basis of the submillimeter colors, we attribute to CO($J = 3\rightarrow2$) at $z = 2.771$. If the emission is instead CO($J = 2\rightarrow1$), then HLock03 would be at $z = 1.514$, although the continuum SED makes this solution unlikely.

SMA interferometry from the compact and very extended array configurations has a combined beam of $1\farcs18 \times 0\farcs97$ and identifies HLock03 as a single submillimeter source (Figure 13). The submillimeter emission is coincident with an IRAC source, but offset by $\sim0\farcs5$ from the galaxy that is detected in both the Keck-II/NIRC2 K_s band and *HST*/WFC3 F110W imaging (Table 3). The K_s-band source is faint, and therefore its redshift is unknown.

The most likely interpretation of these data is that the submillimeter and IRAC data are tracing a background source at $z = 2.771$ that is gravitationally lensed by the K_s-band galaxy. In this case, the absence of prominent detected lensing features means that the magnification of the SMG is likely to be small, and indeed lens modeling of the K_s-band image determines that $\mu = 3.0^{+1.3}_{-1.4}$ for rest-frame optical emission. Therefore, HLock03 is intrinsically luminous, with $L_{IR} \sim 10^{13}\ L_\odot$ and SFR $\sim 1700\ M_\odot\ \mathrm{yr}^{-1}$ (Kennicutt 1998).

6.10. HLock04

Gravitational lensing is confirmed in HLock04, and we have obtained extensive follow-up observations, including Keck-II/NIRC2 K_s-band and *HST*/WFC3 F110W imaging, SMA interferometry, and GBT and CARMA spectroscopy. Gravitationally lensed arcs are evident in the Keck-II, *HST*, and SMA data with an Einstein radius of $2\farcs46$ (Figure 13). The foreground lensing galaxy is detected in SDSS and has a photometric redshift of $z = 0.60 \pm 0.02$ from that survey. Line emission from the lensed SMG was not detected in broadband submillimeter spectroscopy, so the redshift of the SMG is unknown, although the far-IR photometry indicates $z \sim 2$.

HLock04 is unique in our sample, in that the lensing morphology is detected with high significance in both the near- and far-IR wavelength regimes, enabling separate lens modeling of both the stellar and dust emission. Serjeant (2012) showed that differential lensing can be significant for lensed SMGs, due to the irregular distribution of stars, AGNs, gas, and dust in the source plane. Indeed, differential magnification has been identified in two lensed *Herschel* SMGs (Gavazzi et al. 2011; Fu et al. 2012), due to source-plane offsets between the gas, dust, and stellar components.

In the case of HLock04, the SMA data at 880 μm trace the dust emission, which is magnified by $\mu = 5.32^{+1.28}_{-1.06}$. The stellar emission (traced by the K_s-band data) is magnified by $\mu = 6.17 \pm 0.03$ and has $R_{eff} = 0\farcs171 \pm 0\farcs004 = 1.33 \pm 0.03$ kpc in the source plane. The SMA data constrain the size of the emitting dust to $R_{eff} < 0\farcs5$ (<3.9 kpc). Therefore, the stellar and dust models are consistent, and we find no significant differential magnification in HLock04, at least for dust and stellar emission.

6.11. HXMM01

SMA interferometry, coupled with optical imaging, shows that HXMM01 is gravitationally lensed by two galaxies to the east and west of the submillimeter emission (Figure 13). Due to this unique configuration, we have obtained extensive follow-up observations of HXMM01, which will be published in detail in H. Fu et al. (2012, in preparation); here we summarize those results.

Keck-I/LRIS spectroscopy reveals that the eastern and western lensing galaxies are at $z = 0.655$ and $z = 0.502$, respectively, and are thus not physically associated. CO spectroscopy of the CO $J = 1\rightarrow0$, $3\rightarrow2$, and $4\rightarrow3$ transitions shows that HXMM01 is at $z = 2.307$. We have also observed HXMM01 with the F110W filter on *HST*/WFC3; these data are deeper, but lower resolution, than the Keck-I/LRIS imaging. The *HST* imaging is consistent with the Keck data but also reveals the presence of extended emission around the eastern lensing galaxy. This extended emission is inconsistent with being lensed emission from either of the two submillimeter sources, although it may be lensed emission from a third submillimeter-faint galaxy. It is also possible that this extended emission originates from spiral structure in the foreground galaxy.

HXMM01 is a unique case in that the existing follow-up data clearly show that it is made up of two individual, although interacting, SMGs in the source plane. For example, Hα is detected in Keck-II/NIRSPEC long-slit spectroscopy with a 700 km s^{-1} velocity difference between the northern and southern components. The CO($J = 1\rightarrow0$) data also exhibit resolved velocity structure between the two components of the same velocity difference, further supporting a scenario in which the two peaks of SMA emission are two distinct sources separated by $2\farcs8$ (23 kpc at $z = 2.3$). Lens modeling with two separate sources shows that the northern source is lensed by a factor of $\sim$2.1 and the southern source by a factor of $\sim$1.6, for a total of $\sim$3.7. No multiple images are predicted. The optical Hα and [N II] emission lines are broadened in both components of HXMM01 and may trace AGN emission in both galaxies.

6.12. HXMM02

HXMM02 is the brightest source in 1.1 mm AzTEC observations of the Subaru/*XMM-Newton* Deep Field (SXDF), and as such it is also known as SXDF1100.001 or Orochi (Ikarashi et al. 2011). The source is also bright at 250, 350, and 500 μm, with respective flux densities of 190 ± 7, 192 ± 8, and 132 ± 7 mJy in the three SPIRE bands.

Ikarashi et al. (2011) derived a photometric redshift of $z_{phot} = 3.4^{+0.7}_{-0.5}$ for HXMM02, using continuum measurements at 880–1500 μm and in the radio at 20 and 50 cm. We have since obtained additional submillimeter spectroscopy and detected CO($J = 1\rightarrow0$) (GBT; H. Inoue et al. 2012, in preparation), CO($J = 3\rightarrow2$) (CARMA; D. Riechers et al. 2012, in preparation), CO($J = 4\rightarrow3$) (PdBI), and CO($J = 5\rightarrow4$) (CARMA; D. Riechers et al. 2012, in preparation), which pinpoint HXMM02 at $z = 3.395$. We note that there is an additional CO($J = 4\rightarrow3$) measurement obtained with the NRO 45 m telescope (Iono et al. 2012).

HXMM02 is in the SXDF region of the XMM-LSS SWIRE field, and therefore deep Subaru SuprimeCam and UKIRT WFCAM imaging is available (Furusawa et al. 2008; Warren et al. 2007). Ikarashi et al. (2011) showed that a faint optical galaxy, with $z_{phot} = 1.39 \pm 0.01$, is located $0\farcs5$ from the submillimeter centroid. We have since obtained near-IR spectroscopy

with the Infrared Spectrometer and Array Camera on the Very Large Telescope and detect Hα at $z = 1.33$. The positional offset between the optical and the submillimeter sources, coupled with the redshift difference, is indicative of an SMG being gravitationally lensed by the optical galaxy.

HXMM02 has also been imaged with NIRC2 and the Keck-II AO system (Figure 13). No arcs or other morphological indications of gravitational lensing are observed, which is similar to HBoötes01 and HLSJ091828.6+514223 (Combes et al. 2012). Modeling of the SMA data derives a magnification of $\mu = 1.5^{+1.0}_{-0.4}$ for HXMM02. The apparent 8–1000 μm luminosity of HXMM02 is $\mu L_{\rm IR} = (3.6^{+0.3}_{-0.2}) \times 10^{13}\,L_{\odot}$ (Figure 14); thus, the modest amplification from lensing means that the intrinsic luminosity (magnification corrected) is $L_{\rm IR} = (2.4^{+0.6}_{-1.5}) \times 10^{13}\,L_{\odot}$. HXMM02 is an extreme source, even once the effect of gravitational lensing has been accounted for. If the far-IR emission is dominated by star formation, it has intrinsic (lensing-corrected) SFR $\sim 4000\,{\rm M}_{\odot}\,{\rm yr}^{-1}$ (Kennicutt 1998).

6.13. HXMM03

A single line is tentatively detected in CARMA spectroscopy of HXMM03, which, due to the submillimeter photometric redshift, we consider to be CO($J = 3\rightarrow2$) at $z = 2.72$ (D. Riechers et al. 2012, in preparation). High-resolution submillimeter and radio interferometry is not available, and therefore the SMG cannot be pinpointed. No gravitational lensing features are detected in the *HST*/WFC3 F110W imaging, and without an accurate location for the submillimeter emission we are unable to determine whether or not HXMM03 is gravitationally lensed.

7. CONCLUSIONS

We used *Herschel*-SPIRE photometry from the HerMES survey to investigate the nature and prevalence of SMGs that are magnified by strong galaxy–galaxy gravitational lensing, where we consider strong lensing as that with magnification factor $\mu \geqslant 2$. The main results are as follows:

1. We have identified 13 candidate strongly lensed SMGs with $S_{500} \geqslant 100$ mJy in 94.8 deg^2 of blank-field HerMES data ($0.14 \pm 0.04\,{\rm deg}^{-2}$). We also identified a supplementary sample of 29 candidates ($0.31 \pm 0.06\,{\rm deg}^{-2}$) with $S_{500} =$ 80–100 mJy, which have a higher rate of contamination from intrinsically luminous galaxies.
2. Extensive follow-up data for nine (70%) of the sources showed that all nine are strongly gravitationally lensed, with magnification factors of $\mu \sim 2$–23. Our sample, in combination with data from H-ATLAS (Negrello et al. 2010), demonstrates that $\gtrsim$80% of candidates with $S_{500} \geqslant$ 100 mJy are strongly lensed.
3. We showed that the candidate gravitationally lensed sources have red submillimeter colors, indicative of a high-redshift population. Indeed, follow-up data confirm that most of the lensed galaxies are at $z = 2$–4, with apparent 8–1000 μm luminosities of $\mu L_{\rm IR} > 10^{13}\,L_{\odot}$. Thus, if any of these sources are not magnified by gravitational lensing, then they trace some of the most extreme episodes of star formation in the universe.
4. We created a simple statistical model of the gravitational lensing of SMGs by a distribution of foreground masses. The model reproduces the observed 500 μm number counts in HerMES and, independent of the analysis of follow-up data, predicts that 32%–74% of our candidates are strongly gravitationally lensed.
5. The model predicts that the mean magnification of strongly lensed *Herschel*-selected galaxies is a factor of $\sim$7 and $\sim$15 for galaxies with $S_{500} = 100$ and 200 mJy, respectively. Gravitationally lensed SMGs are predicted to have broad distribution of intrinsic (unlensed) 500 μm flux densities with a peak at $\sim$5 mJy, with 65% of sources being intrinsically fainter than 30 mJy at 500 μm. Thus, samples of gravitationally lensed SMGs enable the detailed study of high-redshift, star-forming galaxies, $\sim$65% of which would otherwise be too faint to detect.

While this paper is based on existing HerMES data, planned extragalactic imaging programs with *Herschel*-SPIRE will cover $\sim$1000 deg^2 prior to the end of the mission. Thus, with the method described here, *Herschel* will identify $\sim$150 lensed galaxy candidates at $z \sim 2$–4. With a sample of that size and a selection function that is easily described, it may be possible to perform new fundamental cosmological tests (e.g., Cooray et al. 2010b). Furthermore, these sources are ideal candidates for high-resolution follow-up studies with ALMA and other facilities, enabling us to study the detailed physical conditions in intrinsically faint, star-forming galaxies at high redshift.

We thank Elisabetta Valiante for providing the redshift distributions from her model and an anonymous referee for thoughtful feedback.

SPIRE has been developed by a consortium of institutes led by Cardiff University (UK) and including University of Lethbridge (Canada); NAOC (China); CEA, LAM (France); IFSI, University of Padua (Italy); IAC (Spain); Stockholm Observatory (Sweden); Imperial College London, RAL, UCL-MSSL, UKATC, University of Sussex (UK); and Caltech, JPL, NHSC, University of Colorado (USA). This development has been supported by national funding agencies CSA (Canada); NAOC (China); CEA, CNES, CNRS (France); ASI (Italy); MCINN (Spain); SNSB (Sweden); STFC, UKSA (UK); and NASA (USA).

This research has made use of data from the HerMES project (http://hermes.sussex.ac.uk/). HerMES is a Herschel Key Programme utilizing Guaranteed Time from the SPIRE instrument team, ESAC scientists, and a mission scientist. HerMES is described in Oliver et al. (2012). The data presented in this paper will be released through the HerMES Database in Marseille, HeDaM (http://hedam.oamp.fr/HerMES/).

J.L.W., A.C., F.d.B., C.F., S.K., H.F., and J.C. acknowledge partial support from NSF CAREER AST-0645427 (to A.C. at UCI). S.J.O., L.W., and A.S. acknowledge support from the Science and Technology Facilities Council (grant No. ST/F002858/1 and grant No. ST/I000976/1) at U. of Sussex. A.F., G.M., L.M., and M.V. were supported by the Italian Space Agency (ASI "Herschel Science" Contract I/005/07/0). D.R. acknowledges support from NASA through a Spitzer Space Telescope grant.

Support for program numbers GO-12194 and GO-12488 was provided by NASA through a grant from the Space Telescope Science Institute, which is operated by the Association of Universities for Research in Astronomy, Incorporated, under NASA contract NAS5-26555.

Some of the data presented herein were obtained at the W. M. Keck Observatory, which is operated as a scientific partnership among the California Institute of Technology, the University of California, and the National Aeronautics and Space Administration. The Observatory was made possible by the generous financial support of the W. M. Keck Foundation.

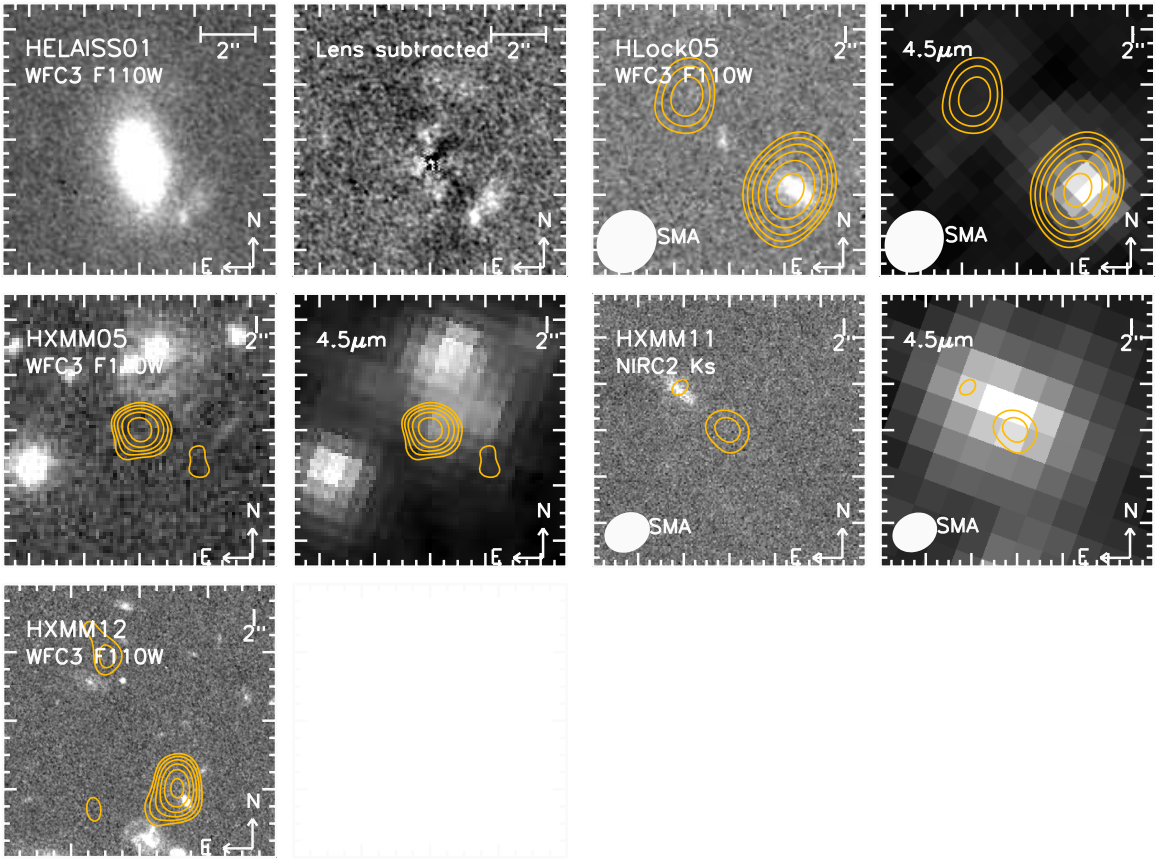

Figure 15. Images of the five supplementary sources with significant follow-up data (the Appendix). Data and contours are as in Figure 13.
(A color version of this figure is available in the online journal.)

The authors recognize and acknowledge the very significant cultural role and reverence that the summit of Mauna Kea has always had within the indigenous Hawaiian community. We are most fortunate to have the opportunity to conduct observations from this mountain.

The Submillimeter Array is a joint project between the Smithsonian Astrophysical Observatory and the Academia Sinica Institute of Astronomy and Astrophysics and is funded by the Smithsonian Institution and the Academia Sinica.

Support for CARMA construction was derived from the Gordon and Betty Moore Foundation; the Kenneth T. and Eileen L. Norris Foundation; the James S. McDonnell Foundation; the Associates of the California Institute of Technology; the University of Chicago; the states of California, Illinois, and Maryland; and the National Science Foundation. Ongoing CARMA development and operations are supported by the National Science Foundation under a cooperative agreement and by the CARMA partner universities.

The National Radio Astronomy Observatory is a facility of the National Science Foundation operated under cooperative agreement by Associated Universities, Inc.

Based on observations carried out with the IRAM Plateau de Bure Interferometer. IRAM is supported by INSU/CNRS (France), MPG (Germany), and IGN (Spain).

This research has made use of the NASA/IPAC Extragalactic Database (NED), which is operated by the Jet Propulsion Laboratory, California Institute of Technology, under contract with the National Aeronautics and Space Administration.

Based on observations made with the Gran Telescopio Canarias (GTC), installed in the Spanish Observatorio del Roque de los Muchachos of the Instituto de Astrofsica de Canarias, in the island of La Palma. The GTC observations are part of the International Time Programme 2010–2011 (PI: PerezFournon).

Facilities: Herschel (SPIRE), CARMA, GBT (Zpectrometer), VLA, Keck:II (NIRC2), Keck:I (LRIS), SMA, IRAM:Interferometer, IRAM:30m, HST (WFC3), Spitzer (IRAC, MIPS), GTC (OSIRIS)

APPENDIX

SUPPLEMENTARY SOURCES

In Table 4, we present 29 supplementary candidate gravitationally lensed SMGs with $S_{500} = 80$–100 mJy. These 29 sources have lower fidelity than the principal sample of 13 candidates with $S_{500} \geqslant 100$ mJy. Five of the supplementary lensed candidates have sufficient follow-up data for detailed study. These five sources are discussed here, and images and SEDs are presented in Figures 15 and 16, respectively. Of the five supplementary candidates, two are confirmed to be gravitationally lensed (HELAISS01 and HXMM11), one is intrinsically luminous (HXMM05), and one is likely to be composed of multiple sources blended in the *Herschel* beam (HXMM12). The final source (HLock05) is likely to be gravitationally lensed, but we cannot confirm this or exclude blending as its origin.

A.1. HELAISS01

We have obtained *HST*/WFC3 F110W imaging of HELAISS01 (Figure 15), which reveals the presence of arc-like

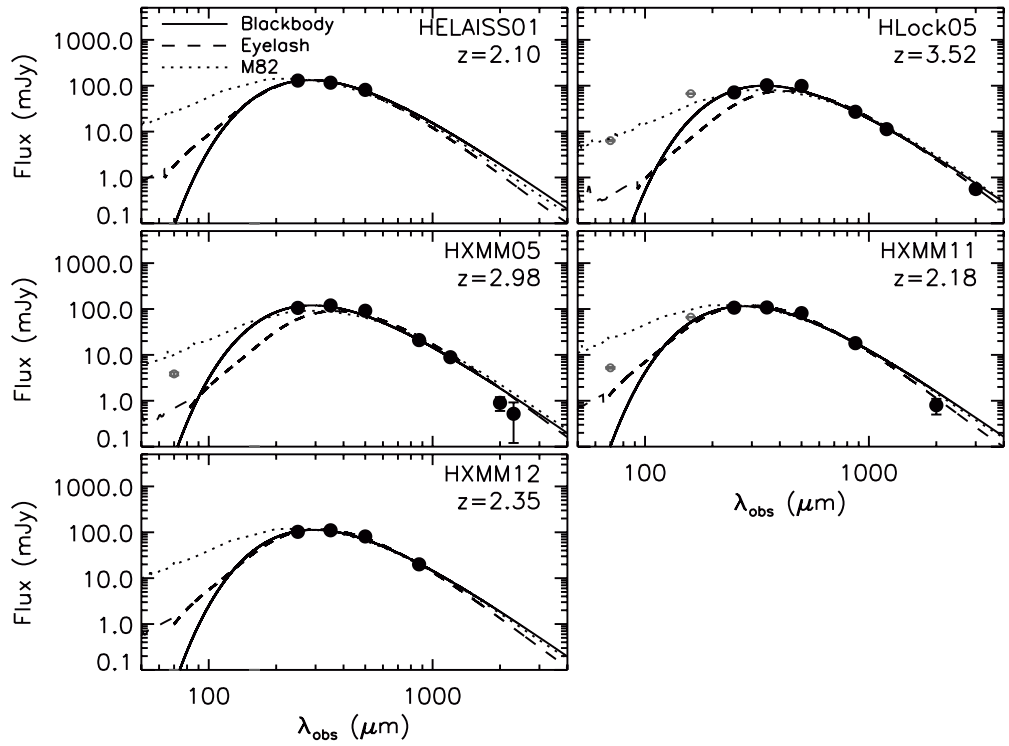

Figure 16. Observed-frame far-IR SEDs of the five supplementary sources with significant follow-up data (the Appendix). As in Figure 14, the far-IR photometry is from HerMES SPIRE data and our extensive follow-up programs (Section 5), and we show the best-fit optically thin modified blackbody SEDs ($\beta = 1.5$), together with M82 (Silva et al. 1998) and the "Cosmic Eyelash" (SMM J2135−0102; Ivison et al. 2010b; Swinbank et al. 2010). The 70 and 160 μm photometry is not used in the fitting.

structures around a foreground source. No other follow-up data are available, and unfortunately, HELAISS01 is located near the edge of the field and the only archival data available are SWIRE 70 μm imaging, in which nothing is detected. The SPIRE emission from HELAISS01 has a submillimeter photometric redshift of $z \sim 2.10$ (Figure 16).

A.2. HLock05

Contours from SMA compact configuration observations of HLock05 are shown overlaid on *HST*/WFC3 F110W imaging in Figure 15. Two submillimeter sources are detected at 870 μm; one of these sources is coincident with an IRAC and F110W galaxy, whereas the other is below the detection threshold of both data sets. There is an optical source between the two SMA peaks, which may be a foreground lens, although it is faint. We have obtained CARMA spectroscopy of HLock05, in which one emission line is clearly detected, which is most likely CO($J = 4\rightarrow3$) at $z = 3.52$.

The two submillimeter sources identified with the SMA may have different colors—the southernmost source is optically bright and detected by IRAC, but the northernmost sources are undetected in the F110W data and marginally detected at 4.5 μm. If these are two images of the same lensed source, the flux ratios in the SMA data are such that a detection of the northernmost source is expected in both the *HST* and the IRAC data. Due to the depths of the data, the apparent color difference is marginal and insufficient to exclude a lensing origin for this source, particularly because differential magnification (e.g., Fu et al. 2012) or an SMG merger may be involved. We are therefore unable to conclusively determine the nature of HLock05. It is most likely to be a gravitationally lensed complex source at $z = 3.52$, although it may also be a blend of two unassociated SMGs.

A.3. HXMM05

We have obtained submillimeter interferometry of HXMM05 with the SMA and high-resolution F110W imaging with *HST*/WFC3. As shown in Figure 15, a single unresolved source is detected in the SMA data. The submillimeter source is detected in the IRAC data, and it is offset by $\sim 2''$ from a resolved optical and near-IR galaxy. The SMG redshift is determined to be $z = 2.985$ with the detection of CO emission lines by CARMA and PdBI. The redshift of the optical galaxy is unknown, but the separations between the two sources and the absence of a lensed SMG counter-image are sufficient to rule out significant magnification. Therefore, we conclude that HXMM05 is a single, unlensed but intrinsically luminous SMG. It has $L_{\rm IR} = (3.2 \pm 0.4) \times 10^{13}\, L_{\odot}$ (SFR $\sim$ 5500 $M_{\odot}\,{\rm yr}^{-1}$; Kennicutt 1998) and $T_{\rm D} = 45 \pm 1$ K, for $\beta = 1.5$.

A.4. HXMM11

HXMM11 is the only source in the supplementary candidate list for which we currently have evidence indicating that it is strongly gravitationally lensed. The configuration is shown in Figure 15, and the SED is in Figure 16. Two faint sources are resolved in SMA interferometric observations, the fainter of which is coincident with a faint $K_{\rm s}$-detected source. The combined centroid of the two SMA galaxies is coincident with an IRAC source, which is most likely the foreground lens. However, the resolution of IRAC is insufficient for this interpretation to be robust. CO($J = 3\rightarrow2$) at $z \sim 2.18$ is observed by CARMA, and corresponding CO($J = 1\rightarrow0$) is detected by the GBT.

A.5. HXMM12

Two SMGs, separated by $\sim 11''$, are detected in SMA interferometry of HXMM12, and no central lensing galaxy is visible in the *HST*/WFC3 F110W imaging. On the basis of this spatial configuration we conclude that HXMM12 is most likely a blend of the two SMGs in the *Herschel*-SPIRE beam. No spectroscopy is available for this source, and if it is a blend of multiple SMGs, then the submillimeter photometric redshift is unreliable.

REFERENCES

Abdo, A. A., Ackermann, M., Ajello, M., et al. 2009, ApJS, 183, 46
Ashby, M. L. N., Stern, D., Brodwin, M., et al. 2009, ApJ, 701, 428
Auger, M. W., Treu, T., Bolton, A. S., et al. 2010, ApJ, 724, 511
Barger, A. J., Cowie, L. L., & Sanders, D. B. 1999, ApJL, 518, 5
Barnabè, M., Auger, M. W., Treu, T., et al. 2010, MNRAS, 406, 2339
Bartelmann, M. 2010, CQGra, 27, 233001
Becker, R. H., White, R. L., & Helfand, D. J. 1995, ApJ, 450, 559
Béthermin, M., Dole, H., Lagache, G., Le Borgne, D., & Penin, A. 2011, A&A, 529, A4
Blain, A. W. 1996, MNRAS, 283, 1340
Blain, A. W., Moller, O., & Maller, A. H. 1999a, MNRAS, 303, 423
Blain, A. W., Smail, I., Ivison, R. J., & Kneib, J. 1999b, MNRAS, 302, 632
Bolton, A. S., Brownstein, J. R., Kochanek, C. S., et al. 2012, ApJ, 757, 82
Bolton, A. S., Burles, S., Koopmans, L. V. E., Treu, T., & Moustakas, L. A. 2006, ApJ, 638, 703
Bolton, A. S., Burles, S., Koopmans, L. V. E., et al. 2008a, ApJ, 682, 964
Bolton, A. S., Treu, T., Koopmans, L. V. E., et al. 2008b, ApJ, 684, 248
Borys, C., Blain, A. W., Dey, A., et al. 2006, ApJ, 636, 134
Browne, I. W. A., Wilkinson, P. N., Jackson, N. J. F., et al. 2003, MNRAS, 341, 13
Brownstein, J. R., Bolton, A. S., Schlegel, D. J., et al. 2012, ApJ, 744, 41
Bullock, J. S., Kolatt, T. S., Sigad, Y., et al. 2001, MNRAS, 321, 559
Carlstrom, J. E., Ade, P. A. R., Aird, K. A., et al. 2011, PASP, 123, 568
Casey, C. M., Berta, S., Béthermin, M., et al. 2012, arXiv:1210.4928
Clements, D. L., Rigby, E., Maddox, S., et al. 2010, A&A, 518, L8
Combes, F., Rex, M., Rawle, T. D., et al. 2012, A&A, 538, L4
Condon, J. J., Cotton, W. D., Greisen, E. W., et al. 1998, AJ, 115, 1693
Conley, A., Cooray, A., Vieira, J. D., et al. 2011, ApJL, 732, 35
Cooray, A., Amblard, A., Wang, L., et al. 2010a, A&A, 518, L22
Cooray, A., Eales, S., Chapman, S., et al. 2010b, arXiv:1007.3519
Cooray, A., & Sheth, R. 2002, PhR, 372, 1
Coppin, K., Chapin, E. L., Mortier, A. M. J., et al. 2006, MNRAS, 372, 1621
Cox, P., Krips, M., Neri, R., et al. 2011, ApJ, 740, 63
Dalal, N., & Kochanek, C. S. 2002, ApJ, 572, 25
de Vries, W. H., Morganti, R., Röttgering, H. J. A., et al. 2002, AJ, 123, 1784
de Vries, W. H., O'Dea, C. P., Barthel, P. D., et al. 2000, AJ, 120, 2300
de Zotti, G., Ricci, R., Mesa, D., et al. 2005, A&A, 431, 893
Desai, V., Armus, L., Soifer, B. T., et al. 2006, ApJ, 641, 133
Diolaiti, E., Bendinelli, O., Bonaccini, D., et al. 2000, A&AS, 147, 335
Dunne, L., Eales, S., Edmunds, M., et al. 2000, MNRAS, 315, 115
Eales, S., Dunne, L., Clements, D., et al. 2010, PASP, 122, 499
Ferkinhoff, C., Brisbin, D., Nikola, T., et al. 2011, ApJL, 740, 29
Frayer, D. T., Harris, A. I., Baker, A. J., et al. 2011, ApJL, 726, 22
Fu, H., Jullo, E., Cooray, A., et al. 2012, ApJ, 753, 134
Furusawa, H., Kosugi, G., Akiyama, M., et al. 2008, ApJS, 176, 1
Gavazzi, R., Cooray, A., Conley, A., et al. 2011, ApJ, 738, 125
Gavazzi, R., Treu, T., Koopmans, L. V. E., et al. 2008, ApJ, 677, 1046
Gavazzi, R., Treu, T., Rhodes, J. D., et al. 2007, ApJ, 667, 176
Gelman, A., & Rubin, D. 1992, StaSc, 7, 457
Gladders, M. D., Rigby, J. R., Sharon, K., et al. 2012, arXiv:1202.5269
Glenn, J., Conley, A., Bthermin, M., et al. 2010, MNRAS, 409, 109
González-Nuevo, J., de Zotti, G., Andreani, P., et al. 2010, A&A, 518, L38
González-Nuevo, J., Lapi, A., Fleuren, S., et al. 2012, ApJ, 749, 65
Griffin, M. J., Abergel, A., Abreu, A., et al. 2010, A&A, 518, L3
Gunn, J. E., & Gott, J. R., III 1972, ApJ, 176, 1
Hailey-Dunsheath, S., Nikola, T., Stacey, G. J., et al. 2010, ApJL, 714, 162
Harris, A. I., Baker, A. J., Frayer, D. T., et al. 2012, ApJ, 752, 152
Harris, A. I., Baker, A. J., Jewell, P. R., et al. 2007, in ASP Conf. Ser. 375, From Z-Machines to ALMA: (Sub)Millimeter Spectroscopy of Galaxies, ed. A. J. Baker, J. Glenn, A. I. Harris, J. G. Mangum, & M. S. Yun (San Francisco, CA: ASP), 82
Hewitt, A., & Burbidge, G. 1989, ApJS, 69, 1
Hezaveh, Y. D., & Holder, G. P. 2011, ApJ, 734, 52
Hezaveh, Y. D., Marrone, D. P., & Holder, G. P. 2012, ApJ, 761, 20
Hopwood, R., Wardlow, J., Cooray, A., et al. 2011, ApJL, 728, 4
Ikarashi, S., Kohno, K., Aguirre, J. E., et al. 2011, MNRAS, 415, 3081
Iono, D., Hatsukade, B., Kohno, K., et al. 2012, PASJ, 64, L2
Iono, D., Peck, A. B., Pope, A., et al. 2006a, ApJL, 640, 1
Iono, D., Tamura, Y., Nakanishi, K., et al. 2006b, PASJ, 58, 957
Ivison, R. J., Magnelli, B., Ibar, E., et al. 2010a, A&A, 518, L31
Ivison, R. J., Papadopoulos, P. P., Smail, I., et al. 2011, MNRAS, 412, 1913
Ivison, R. J., Swinbank, A. M., Swinyard, B., et al. 2010b, A&A, 518, L35
Jackson, C. A., Wall, J. V., Shaver, P. A., et al. 2002, A&A, 386, 97
Jackson, N., & Browne, I. W. A. 2007, MNRAS, 374, 168
Jain, B., & Lima, M. 2011, MNRAS, 411, 2113
Jannuzi, B. T., & Dey, A. 1999, in ASP Conf. Ser. 191, Photometric Redshifts and the Detection of High Redshift Galaxies, ed. R. Weymann, L. Storrie-Lombardi, M. Sawicki, & R. Brunner (San Francisco, CA: ASP), 111
Kennicutt, R. C., Jr. 1998, ARA&A, 36, 189
Kochanek, C. S. 1995, ApJ, 445, 559
Komatsu, E., Smith, K. M., Dunkley, J., et al. 2011, ApJS, 192, 18
Koopmans, L. V. E., Bolton, A., Treu, T., et al. 2009, ApJL, 703, 51
Koopmans, L. V. E., Treu, T., Bolton, A. S., Burles, S., & Moustakas, L. A. 2006, ApJ, 649, 599
Kormendy, J. 1977, ApJ, 218, 333
Lacey, C., & Cole, S. 1993, MNRAS, 262, 627
Lagache, G., Dole, H., & Puget, J.-L. 2003, MNRAS, 338, 555
Lapi, A., Negrello, M., González-Nuevo, J., et al. 2012, ApJ, 755, 46
Levenson, L., Marsden, G., Zemcov, M., et al. 2010, MNRAS, 409, 83
Lewis, A., & Bridle, S. 2002, PhRvD, 66, 103511
Lima, M., Jain, B., & Devlin, M. 2010a, MNRAS, 406, 2352
Lima, M., Jain, B., Devlin, M., & Aguirre, J. 2010b, ApJL, 717, 31
Lindner, R. R., Baker, A. J., Omont, A., et al. 2011, ApJ, 737, 83
Lonsdale, C. J., Smith, H. E., Rowan-Robinson, M., et al. 2003, PASP, 115, 897
Lupu, R. E., Scott, K. S., Aguirre, J. E., et al. 2012, ApJ, 757, 135
Marshall, P. J., Hogg, D. W., Moustakas, L. A., et al. 2009, ApJ, 694, 924
Marshall, P. J., Treu, T., Melbourne, J., et al. 2007, ApJ, 671, 1196
Massaro, E., Giommi, P., Leto, C., et al. 2009, A&A, 495, 691
Mayer, A., Jorissen, A., Kerschbaum, F., et al. 2011, A&A, 531, L4
Metcalf, R. B., & Zhao, H. 2002, ApJL, 567, 5
Miralda-Escude, J. 1995, ApJ, 438, 514
More, A., Cabanac, R., More, S., et al. 2012, ApJ, 749, 38
Navarro, J. F., Frenk, C. S., & White, S. D. M. 1997, ApJ, 490, 493
Negrello, M., Hopwood, R., De Zotti, G., et al. 2010, Sci, 330, 800
Negrello, M., Perrotta, F., González-Nuevo, J., et al. 2007, MNRAS, 377, 1557
Oguri, M., Inada, N., Pindor, B., et al. 2006, AJ, 132, 999
Oguri, M., Inada, N., Strauss, M. A., et al. 2012, AJ, 143, 120
Oliver, S. J., Bock, J., Altieri, B., et al. 2012, MNRAS, 424, 1614
Oliver, S. J., Wang, L., Smith, A. J., et al. 2010, A&A, 518, L21
Omont, A., Beelen, A., Bertoldi, F., et al. 2003, A&A, 398, 857
Omont, A., Neri, R., Cox, P., et al. 2011, A&A, 530, L3
Oyaizu, H., Lima, M., Cunha, C. E., et al. 2008, ApJ, 674, 768
Paciga, G., Scott, D., & Chapin, E. L. 2009, MNRAS, 395, 1153
Patanchon, G., Ade, P. A. R., Bock, J. J., et al. 2009, ApJ, 707, 1750
Peacock, J. A. 1982, MNRAS, 199, 987
Perley, R. A., Chandler, C. J., Butler, B. J., & Wrobel, J. M. 2011, ApJL, 739, 1
Perrotta, F., Baccigalupi, C., Bartelmann, M., De Zotti, G., & Granato, G. L. 2002, MNRAS, 329, 445
Pilbratt, G. L., Riedinger, J. R., Passvogel, T., et al. 2010, A&A, 518, L1
Refregier, A., & Loeb, A. 1997, ApJ, 478, 476
Richard, J., Jones, T., Ellis, R., et al. 2011, MNRAS, 413, 643
Richard, J., Stark, D. P., Ellis, R. S., et al. 2008, ApJ, 685, 705
Riechers, D. A., Cooray, A., Omont, A., et al. 2011a, ApJL, 733, 12
Riechers, D. A., Hodge, J., Walter, F., Carilli, C. L., & Bertoldi, F. 2011b, ApJL, 739, 31
Riechers, D. A., Walter, F., Brewer, B. J., et al. 2008, ApJ, 686, 851
Roseboom, I. G., Ivison, R. J., Greve, T. R., et al. 2012, MNRAS, 419, 2758
Roseboom, I. G., Oliver, S. J., Kunz, M., et al. 2010, MNRAS, 409, 48
Ruff, A. J., Gavazzi, R., Marshall, P. J., et al. 2011, ApJ, 727, 96
Rusin, D., & Kochanek, C. S. 2005, ApJ, 623, 666
Sault, R. J., Teuben, P. J., & Wright, M. C. H. 1995, in ASP Conf. Ser. 77, Astronomical Data Analysis Software and Systems IV, ed. R. A. Shaw, H. E. Payne, & J. J. E. Hayes (San Francisco, CA: ASP), 433
Schechter, P. 1976, ApJ, 203, 297
Scott, K. S., Lupu, R. E., Aguirre, J. E., et al. 2011, ApJ, 733, 29
Scott, S. E., Dunlop, J. S., & Serjeant, S. 2006, MNRAS, 370, 1057
Serjeant, S. 2012, MNRAS, 424, 2429
Serjeant, S., & Harrison, D. 2005, MNRAS, 356, 192
Sheth, R. K., & Tormen, G. 1999, MNRAS, 308, 119
Short, J., Pearson, E., Coles, P., & Eales, S. 2012, arXiv:1206.4919

Silva, L., Granato, G. L., Bressan, A., & Danese, L. 1998, ApJ, 509, 103
Smith, A. J., Wang, L., Oliver, S. J., et al. 2012, MNRAS, 419, 377
Stacey, G. J., Hailey-Dunsheath, S., Ferkinhoff, C., et al. 2010, ApJ, 724, 957
Stark, D. P., Ellis, R. S., Richard, J., et al. 2007, ApJ, 663, 10
Stocke, J. 1979, ApJ, 230, 40
Sturm, E., Verma, A., Graci-Carpio, J., et al. 2010, A&A, 518, L36
Suyu, S. H., Marshall, P. J., Hobson, M. P., & Blandford, R. D. 2006, MNRAS, 371, 983
Swinbank, A. M., Chapman, S. C., Smail, I., et al. 2006, MNRAS, 371, 465
Swinbank, A. M., Papadopoulos, P. P., Cox, P., et al. 2011, ApJ, 742, 11
Swinbank, A. M., Smail, I., Longmore, S., et al. 2010, Natur, 464, 733
Swinyard, B. M., Ade, P., Baluteau, J.-P., et al. 2010, A&A, 518, L4
Tacconi, L. J., Neri, R., Chapman, S. C., et al. 2006, ApJ, 640, 228
Takada, M., & Jain, B. 2003, MNRAS, 344, 857
Treu, T. 2010, ARA&A, 48, 87
Treu, T., Auger, M. W., Koopmans, L. V. E., et al. 2010, ApJ, 709, 1195
Treu, T., & Koopmans, L. V. E. 2004, ApJ, 611, 739
Valiante, E., Lutz, D., Sturm, E., Genzel, R., & Chapin, E. L. 2009, ApJ, 701, 1814
Valtchanov, I., Virdee, J., Ivison, R. J., et al. 2011, MNRAS, 415, 3473
Vieira, J. D., Crawford, T. M., Switzer, E. R., et al. 2010, ApJ, 719, 763
Voges, W., Aschenbach, B., Boller, Th., et al. 1999, A&A, 349, 389
Warren, S. J., & Dye, S. 2003, ApJ, 590, 673
Warren, S. J., Hambly, N. C., Dye, S., et al. 2007, MNRAS, 375, 213
Weiß, A., Ivison, R. J., Downes, D., et al. 2009a, ApJL, 705, 45
Weiß, A., Kovács, A., Coppin, K., et al. 2009b, ApJ, 707, 1201
White, R. L., Becker, R. H., Helfand, D. J., & Gregg, M. D. 1997, ApJ, 475, 479
Wizinowich, P. L., Chin, J., Johansson, E., et al. 2006, Proc. SPIE, 6272, 627209
Wright, A. E., Griffith, M. R., Burke, B. F., & Ekers, R. D. 1994, ApJS, 91, 111
Younger, J. D., Fazio, G. G., Wilner, D. J., et al. 2008, ApJ, 688, 59